Kinematic and Emission Analysis of the Relativistic Jet in the Blazar B1551+130 using VLBI Data

SHAUN JULIAN NICOL

MSci Project
IMPERIAL COLLEGE LONDON

Host Institute:
Universitat de València

Supervisor:
Prof. Eduardo Ros Ibarra

June 2012

Abstract

Very Long Baseline Interferometry (VLBI) allows the most energetic structures in our universe to be observed with sub-milliarcsecond resolution (parsecs at cosmological distances). These methods are particularly effective in observing the relativistic jets extending from the black hole region of active galactic nuclei (AGN). Six epochs of VLBI data from the MOJAVE 2 cm survey taken between June 2009 and April 2012 are used to carry out the kinematic analysis of the relativistic jet in the flat spectrum radio quasar B1551+130 with redshift $z = 1.308$. The apparent velocities of areas of enhanced radio emission, or 'knots', in the jet, calculated through the model fitting technique, are presented along with images of the source obtained through the hybrid mapping process. Superluminal velocities for the 'knots' are observed with the highest apparent velocity being 10.2±1.8c. From this maximum velocity, the viewing angle of $5.6^\circ \pm 1^\circ$ is derived, agreeing with the classification of the source as a FSRQ. An estimate of the luminosity Doppler boosting factor gives a value of order 10^2. Two jet features are observed with negative superluminal velocities, the most significant being the region closest to the base or 'core' of the jet observed with a velocity of −10.6±2.7c. The flux of this region undergoes a large increase during the most recent observations, between mid 2011 and mid 2012. No definitive explanations of this phenomenon are able to be given in this work due to the lack of subsequent observations which will allow the nature of the findings to be distinguished. To conclude, the variations in the core flux measured through VLBI are compared with the *Fermi* satellite gamma ray light curve of the source, the results of which point to a possible correlation between radio and gamma flares observed during the period 2010-11.

Resumen

La técnica de VLBI permite observar las estructuras más energéticas de nuestro universo con una resolución angular inferior a un milisegundo de arco (escalas de pársec a distancias cosmológicas). Estos métodos son particularmente útiles en la observación de chorros o 'jets' relativistas provenientes del agujero negro central en los núcleos activos de galaxias ('active galactic nuclei' o AGN). Se han utilizado seis observaciones individuales de datos de VLBI del proyecto MOJAVE/2 cm Survey, realizadas entre junio de 2009 y abril de 2012 para estudiar la cinemática del jet relativista del cuásar de espectro plano B1551+130, con desplazamiento al rojo $z = 1.308$. Se presentan tanto las velocidades aparentes de las distintas regiones del 'jet', calculadas con el método de 'model fitting' como las imágenes de la radiofuente producidas con la técnica de cartografiado híbrido o 'hybrid mapping'. Se observan velocidades superlumínicas de las distintas regiones del 'jet', con un valor máximo de $10.2 \pm 1.8c$. A partir de este valor se estima el ángulo máximo del 'jet' respecto a la línea de visión, que resulta ser de $5.6^\circ \pm 1.2^\circ$. Se estima también el factor de reforzamiento Doppler de la luminosidad, que es de orden de magnitud 10^2. Se observan dos regiones en el 'jet' con velocidades aparentes negativas, siendo la más significativa la región más cercana a la base del 'jet' o 'core', con un valor de -10.6 ± 2.7c. El flujo de esta región aumenta de manera significativa durante las dos últimas observaciones, esto es, de mediados de 2011 a mediados de 2012. En este trabajo no podemos dar una explicación definitiva a este fenómeno, a falta de observaciones posteriores que permitan distinguir lo ocurrido. Para concluir, comparamos los restultados obtenidos con VLBI del aumento de brillo en la base del 'jet' con la curva de luz en rayos γ del satélite *Fermi*, datos que apuntan a una posible correlación entre ambos eventos durante el periodo 2010–11.

Contents

Chapter 1

Introduction

"The data give for the coordinates of the region from which the disturbance comes, a right ascension of 18 hours and a declination of –10°"

(Karl G. Jansky, 1933)

In the early 1930's, graduate physicist Karl Janksy was commissioned to measure radio interference levels at 20.5 MHz by a company looking to develop a transatlantic radio telephone service. He noted a strange radio hiss which could not be explained by any climatological effect. Indeed the hiss varied with each sidereal, not solar, day forcing Jansky to look deeper into the night sky to explain the disturbance. Through further observations he concluded the noise emanated from the direction of the centre of the Milky Way, in the sagittarius constellation. Janky, however, could not continue in his investigation of the source as his application for funding to build a 30m dish antenna was rejected by Bell Laboratories whose goals had been realised by Janksy's first experiment. His observations however, would mark the birth of a field of astronomy which now provides mankind with an enormously powerful tool in our quest for understanding what lies in the depths of our universe and how it came to exist.

After Jansky's observations, the practice of observing the sky at radio wavelengths took some time to gather momentum. If, as many believed, the main features in our universe were stellar structures - even the coolest of which emit most strongly in the visible or infrared spectrum - why go to the trouble of constructing large radio antennas?

The discovery of the Hydrogen 21-cm spectral line by Edward Purcell and Harold Ewen was one of the first significant milestones in radio astronomy. The existence of the spectral line was first predicted by Hendrick van de Hulst in 1945 after Dutch astronomer Jan Oort highlighted the need for a spectral line to be found in the radio spectrum. Oort was interested in measuring radial velocities of stars within galaxies to determine their structure and noted the Doppler shift of a radio spectral line would allow for such observations without the interference of interstellar dust.

Unlike observations at other wavelengths, radio astronomy benefits from a lack of atmospheric absorption. Observations in the gamma, X-ray, and UV regions must be carried out above the Earth's atmosphere because of absorption by atmospheric gases. A large window exists however between the submillimeter microwave region and the 10m radio region where the energy flux of EM radiation is affected by the atmosphere to such a small degree that precision astronomy can take place from the ground. At wavelengths longer than around 10m, absorption by the ionosphere starts to become significant, as shown in Fig. 1.1. This window through the atmosphere avoids some practical difficulties, however radio wavelenghts present challenges of their own.

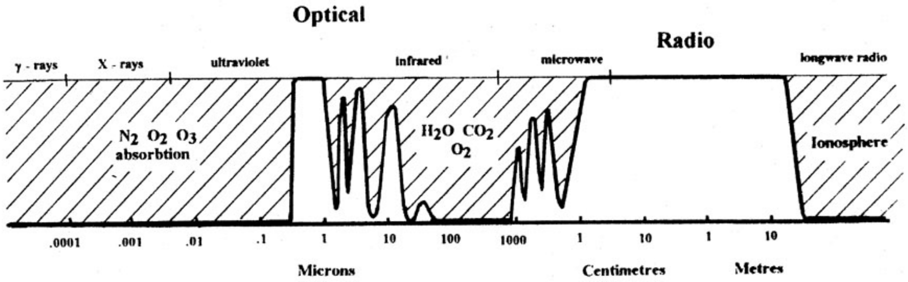

Figure 1.1: [6]. The levels of atmospheric absorption along the EM spectrum. At radio wavelenghts, a large window is evident allowing radio interferometry to be conducted on the ground with high accuracy.

The aim common to all disciplines of astronomy is that of achieving the highest possible angular resolution in order to accurately detect and translate the emission of EM radiation from a source into an image of brightness distribution. For an optical instrument, this limit, known as the diffraction limit, can be expressed in simple terms by

$$\theta \approx \frac{\lambda}{D} \tag{1.1}$$

where θ is the maximum angular resolution (in radians), λ the wavelength which the device detects, and D the diameter of the aperture of the detecting device. For an optical instrument, this resolution limit poses no serious problem since the wavelengths involved are so small that even devices of cm aperture can provide sufficient resolution. However, if we consider the case of detecting radio waves, with wavelengths three to four orders of magnitude higher, it results that to achieve the same angular resolution, our device must be of kilometre scale aperture. Due to the acute impracticality of such devices, it is clear that the future of high resolution radio astronomy could not lie in single aperture instruments.

Throughout the 50's and 60's new techniques were developed to improve the angular resolution in radio astronomy whilst maintaining feasible detection device characteristics. Future observations would rely on the ability to combine signals from separate antennas to increase the effective aperture diameter, and hence angular resolution, in a technique known as Aperture Synthesis. Another major milestone came in 1953 when Walter Baade and Rudolph Minowski observed the first known radio loud galaxy, Cygnus A, using the closure phase method.

Perhaps the most valuable theoretical contribution to radio astronomy to date came in 1962 when Sir Martin Ryle developed the Earth Rotation Synthesis method. Ryle was awarded the Nobel Prize in 1974 for this technique which exploits the changing orientation of baselines formed between pairs of antennas in an array to increase angular resolution. Subsequently, techniques were developed to combine signals from radio antennas positioned thousands of kilometres from each other in a method known as Very Long Baseline Interferometry (VLBI).

With the increase in angular resolution achieved through innovative interferometric techniques came the ability to image the most energetic processes in our universe. Along with radio supernovae, pulsars and other astrophysical phenomena, radio interferometry allowed the observation of Active Galactic Nuclei - immense, highly energetic structures found at the core of distant galaxies, emitting in all bands of the EM spectrum.

This report begins with the description of the properties of Active Galactic Nuclei (AGN), their classification, and the relativistic phenomena associated with energetic radio jets extending from their core (Chapter 2). Chapter 3 deals with the basic interferometric principles which form the basis of radio astronomy before explaining the techniques which allow high angular resolution to be obtained through combining signals from separate antennas. This section also deals with the methods involved in producing maps of brightness distribution of a source and provides a brief summary of the efforts of VLBI in imaging AGN. Chapter 4 gives a brief introduction to the object of study, outlines the method used in producing images of the source and presents these images along with describing the methods used in the kinematic analysis of the relativistic jet of the source. The results of the kinematic analysis are also presented in this section. Chapter 5 evaluates the results of the kinematic analysis and discusses possible explanations of the observations along with presenting some data to describe the emission of the object of study at other wavelengths with particular emphasis on gamma emission and the possible relation between radio and gamma flares. Chapter 6 concludes the report by summarising the topics discussed, the main results, and the hypotheses presented.

Chapter 2

Active Galactic Nuclei and Relativistic Jets

2.1 Active Galactic Nuclei

2.1.1 General Properties

The presence of such remarkable features in our universe was first noted by Carl Seyfert in 1943. He observed a class of galaxies with seemingly star-like unresolved bright cores but which showed very broad optical emission lines. Subsequent observations by other astronomers revealed the presence of other such sources which, when taking into account their redshift, showed remarkably high luminosity ([12], [35], [3]). In 1963, Maarten Schmidt detected the radio source 3C 273 which was shown to have a luminosity of 10^{12} times that of the sun confined to an area the size of the solar system.

Since then many more such sources have been identified, roughly 3% of all galaxies are classified as being active, and there have been many attempts to answer the fundamental questions: what are these sources, and can a model be created to explain their observed properties?

Unlike normal galaxies, AGN show very high variability, their emission can change on timescales of days or even less. The brightest feature in all active galaxies is their core; objects located at large distances very often outshine their host galaxy to the extent that only the nucleus is visible.

Another remarkable property of AGN is their range of EM emission. AGN can cover the full spectrum from gamma to radio, with the intensity of emission in each part of the spectrum also highly variable between sources. Models to unify the structure of all AGN must somehow accommodate for these differences. By taking into account only 2 parameters: strength of radio emission and width of optical lines, a simple classification method can be formulated as shown in Table 2.1.

Galaxies are considered to be radio-loud if the ratio of radio flux at 5GHz to their optical flux in the B band is greater than 10 [29]. Around 10-15% of observed AGN are termed radio-loud, the rest radio-quiet.

At the centre of AGN is thought to lie a black hole of around 10^6 to 10^8 $M_\odot$. The accretion of gas from the ISM, and possibly disturbed stars or other matter, onto the black hole, releases the gravitational potential energy that gives rise to the high luminosities of AGN. This thermal process is thought dominate emission in the radio-quiet case, whereas in radio-loud AGN, powerful relativistic jets of particles extend perpendicularly from the core, giving rise to high radio emissivity through non-thermal syncrotron radiation.

Radio emission	**Optical emission line properties**		
	Type 2 (narrow lines)	**Type 1** (broad lines)	**Type 0** (weak/absent lines)
Radio-quiet:	Seyfert 2	Seyfert 1 QSO	
Radio-loud:	NLRG $\wedge$ (FR I, FR II)	BLRG SSRQ FSRQ	Blazars $\wedge$ (BL Lac, FSRQ)

Table 2.1: Adapted from [29]. AGN classification method based on optical emission line properties and radio luminosity (see below for description of AGN classes). All radio-quiet AGN, which make up 85-90% of observed AGN, show clear optical emission lines. Within Type 2 AGN are Seyfert 2 galaxies and Narrow-Line Radio Galaxies of type FR I and FR II. Type 1 AGN are Seyfert 1 galaxies, Quasi-Stellar Objects, Broad-Line Radio Galaxies, Steep-Spectrum Radio Quasars and Flat-Spectrum Radio Quasars. The Type 0 AGN are BL Lacertae objects and Flat-Spectrum Radio Quasars.

2.1.2 Types of AGN

Radio-quiet AGN

The emission from radio-quiet AGN is dominated by thermal processes and peaks in the optical/UV/soft X-ray region. Within the radio-quiet classification are Seyfert Galaxies and Quasi-Stellar Objects (QSO)

Seyfert Galaxies

The class of galaxies observed by Seyfert in 1943 now bear his name. Seyfert galaxies are radio-quiet, and, depending on their emission lines are classified as Seyfert 2 or Seyfert 1. Seyert 2 galaxies show broad *and* narrow optical emission lines. The doppler-broadened lines correspond to velocities in the region of 10^4 km s^{-1}. Seyfert 1's only show narrow lines. Their host galaxies, usually spiral, are detectable around their bright core.

QSO

Quasi-Stellar Objects, or QSO, get their name from their very luminous, unresolved core. Due to Seyfert 1 galaxies only being observed up to certain redshifts, it is believed they may be intrinsically very similar to

QSO but the latter are located at larger distances which renders their host galaxies undetectable.

Radio-loud AGN

Radio-loud AGN are dominated by non-thermal syncrotron radiation from the core and the relativistic jets. Their optical emission lines, radio spectrum shape, and luminosity, allow them to be categorised as radio galaxies, quasars, and blazars.

Radio Galaxies

There are two types of radio galaxies, which, depending on the width of their optical emission lines, are labelled either Narrow Line Radio Galaxies (NLRG) or Broad Line Radio Galaxies (BLRG). They are distinguished by their optical emission lines. NLRG are Type 2 AGN, showing only narrow lines. The NLRG subclasses FR I and FR II were devised by Fanaroff and Riley in 1974 [10] to distinguish between NLRG with different radio emission morphology along the jets. Both a typical FR I and FR II galaxy are shown in Fig. 2.1. In FR I types, emission from the core and base of the jets dominates the radio spectrum whereas in FR II types, areas of high radio flux, or 'hotspots', exist the in widened extremities of the jets (radio-lobes). In absolute terms, the core and jets of FR II galaxies are more luminous than the FR I type. Jets are detected in around 80% of FR I galaxies. Broad line radio galaxies, BLRG, are of Type 1 AGN and show Doppler broadened emission lines. As is the case for FR II galaxies, the radio emission of BLRG is lobe-dominated.

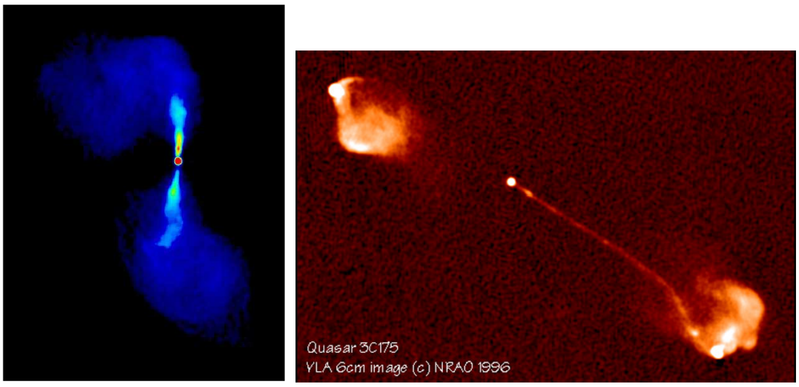

Figure 2.1: **Left:** Radio image of M84 [22], a typical FR I radio galaxy. **Right:** 6cm Radio image of 3C175, a typical FR II galaxy [5].

Quasars

Quasi-stellar radio sources (quasars) are the radio-loud counterparts of QSO. Quasars are the most luminous of all AGN and can have bolometric brightness values of below -21.5 mag (e.g., [40]). Steep spectrum radio quasars, (SSRQ) have radio spectra which correspond to lobe-dominated emission, wheras the spectra of flat spectrum radio quasars (FSRQ) show emission from the core and base of the jets is dominant.

Blazars

Blazars are Type 0 AGN and can be either BL Lacertae objects (BL Lacs) or FSRQ. BL Lacs show very weak optical emission lines hence obtaining their redshift can be difficult. They are very compact structures and have a flat radio spectrum. Their emission is dominated by non-thermal syncrotron radiation associated with core and jets of AGN. FSRQ are classified both as Type 1 and Type 0 AGN as they show strong broad optical emission lines but their multifrequency spectra are dominated, as in BL Lacs, by non-thermal emission.

2.1.3 Unification model

The model to explain the vastly varying emission properties of AGN predicts that all AGN possess similar physical features but their differences arise from their orientation towards the line of sight of the observer. This model, presented by Urry and Padovani in 1995 [37], goes a long way in providing a physical model to better understand AGN, but discrepancies still remain as no physical model has been successful unifying all observed AGN, as discussed at the end of this section.

The main physical features of the model are outlined below and are shown in Fig. 2.2

Black Hole

A black hole, or any mass concentration of around 10^6 to 10^9 solar masses confined to a area around 0.01pc in diameter, lies at the centre of all AGN [6]. The immense mass of the black hole provides the energy in the form of gravitation potential necessary to produce the observed luminosities of AGN.

Accretion disc

This thin disc of ionized material spans a few parsecs at most feeding material into the central black hole. The accretion disc emits thermal radiation and peaks in the optical/UV/soft X-ray region. The temperature varies across the disc and the observed spectral lines are broadened due to rotation and turbulent motion. There tend to be a limited number of spectral lines observed in AGN, predominantly from H, He, C, N, O, Mg, Ne.

Torus

The torus is a large toroidal region of accreting material surrounding the accretion disc which reaches out from around 1.5–30 pc diameter. It is composed of molecular material and its opacity is such that it renders the accretion disc invisible if viewed ‘side on’. The torus emits mainly in Infrared.

Broad Line Region

Although not a physical structure, the broad line region (BLR) describes the area above the accretion disc within the molecular torus. Within the BLR are fast moving clouds of gas, often with velocities in the region of around 10^4 km s^{-1}. The spectral lines are seen to be highly broadened and the continuum radiation from the BLR can extend up to the keV X-ray region.

Narrow Line Region

The narrow line region (NLR) extends beyond the broad line region. Gas clouds contained within it, depicted as purple bubbles in Fig. 2.2, move slower than in the BLR, typically at speeds of the order of 10^2 km s^{-1}.

Hot Electron Corona

The hot electron corona lies in the inner region of the NLR, depicted as black dots in Fig. 2.2. The presence of an hot ionized corona, acting as scattering medium, was deduced from the detection of a low level of BLR optical and X-ray lines in the continuum of a source in which the BLR was not directly detectable through the obscuring torus.

The relativistic jets, being the main focus of this project, are discussed in detail in the next section.

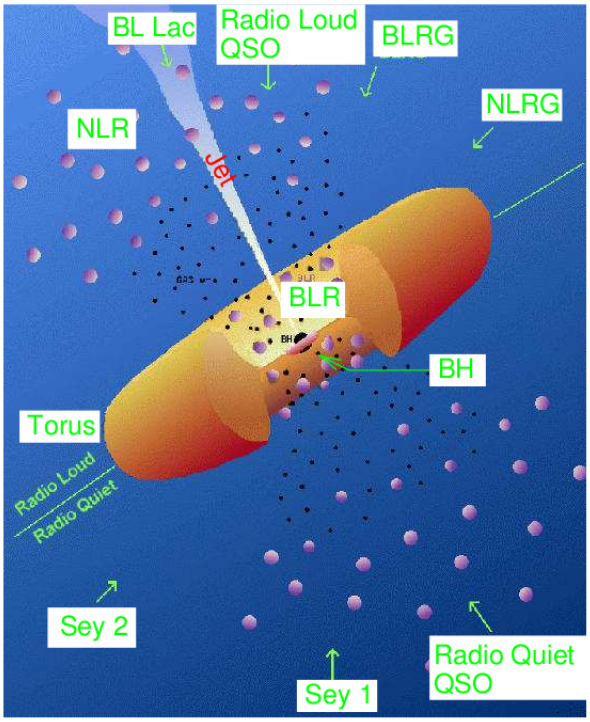

Figure 2.2: [40] adapted [29]. The structure of the unified model of AGN. The central black hole (BH) is surrounded by a small accretion disc. Around the accretion disc lies the large molecular torus. The BLR consists of the gas clouds (purple bubbles) moving within the torus above the core. The NRL extends farther away from the centre. The hot electron corona (black dots) extends from the BLR into the NLR. Also shown are the orientations w.r.t. the line sight for the classes of AGN. In the radio-loud case (with jet) quasars and blazars are orientated at smaller angles than radio galaxies. In the radio-quiet case (bottom end of figure), the small angle of Seyfert 1's and QSO's allows the BLR to be 'seen'.

Successes of the model

The 'unification by orientation' model yields a common picture for some but not all AGN classes. It seems to hold in the radio-quiet case by describing Seyfert 2 galaxies as the small angle equivalents of Seyfert 1's and QSO, since their smaller viewing angle allows the BLR to be seen. The larger angles of Seyfert 2's only allow emission from the NLR to be detected. With an absence of relativistic jets, the emission Seyfert galaxies and QSO is dominated by the thermal process taking place around the core.

In the radio-loud case, the optical lines of NLRG and BLRG can be effectively explained, as in the radio-quiet case, by their orientation with respect to the line of sight. Steep spectrum radio quasars show radio spectra corresponding to lobe-dominated emission, hence, they can only be unified with FR II type radio galaxies at smaller viewing angles. The flat radio spectra of blazars can be explained by the fact they are orientated in a way that the observer is 'looking down' the jet at small angles. This means the radio emission detected is core and jet dominated, as opposed to lobe-dominated. The small angle also explains Doppler boosting effects and apparent superluminal motion of jet components discussed in Section 2.2.2 and leads to BL Lacs and FSRQ having the strongest radio emission of all AGN.

2.2 Relativistic Jets

2.2.1 Emission Properties

As previously mentioned, in radio-loud AGN, jets of material moving at relativistic speeds extend from the polar regions of the black hole region. The collimation and shape of the jets vary from source to source (see Fig. 2.1).

The jets originate from the core of AGN, the intensely bright region at the centre of AGN which emits synchrotron radiation from radio to gamma. In the radio-loud case the core represents the base of the jets. It is the region of the jet with the highest intrinsic brightness temperature. The core brightness temperature T_b can reach values of up to 10^{14}K [20] although typically lies in the region of 10^{11}–10^{12} K.

The core and the jets can be considered continuous and observations show that in most cases, only one jet is visible, and typically extends out to a projected distance of around 100 kpc. It is still to be agreed as to whether this is due to some instrinsic asymmetry or due to other factors such as the Doppler boosting (discussed below) of the dominant jet. The jets (and the core) are dominated by non-thermal syncrotron radiation emitted when high energy charged particles travelling at relativistic speeds accelerate in the weak magnetic field of the jet. Typically, for the charged particels, the Lorentz factor γ has a value of around 1000, and the magenetic field is of around 10 μG [6]. Brightness temperatures typically extend from around 10^{12} K in the core to around 10^{10} K in the jets.

As discussed in [27], the exact processes responsible for the non-thermal radiation are still being debated. Although it is likely that accelerating electrons and positrons are the main source, some evidence has been put forward that normal matter plasma could give rise to such emission [32]. The emission regions of the jet are schematised in Fig. 2.3.

The most energetic AGN jets are responsible as well for gamma emission. Gamma emission is strongest in blazars due to Doppler boosting effects (see below). Out of the AGN detected in gamma surveys, the overwhelming majority are BL Lac objects. The relation between flares in gamma emission and radio jet morphology is currently being investigated by teams cross referencing VLBI observations with data from the Large Area Telescope on board the *Fermi* Gamma Ray Space Telescope. Although it has been suggested that gamma flares correspond to enhanced radio emission, no robust conclusions have yet been drawn from the research.

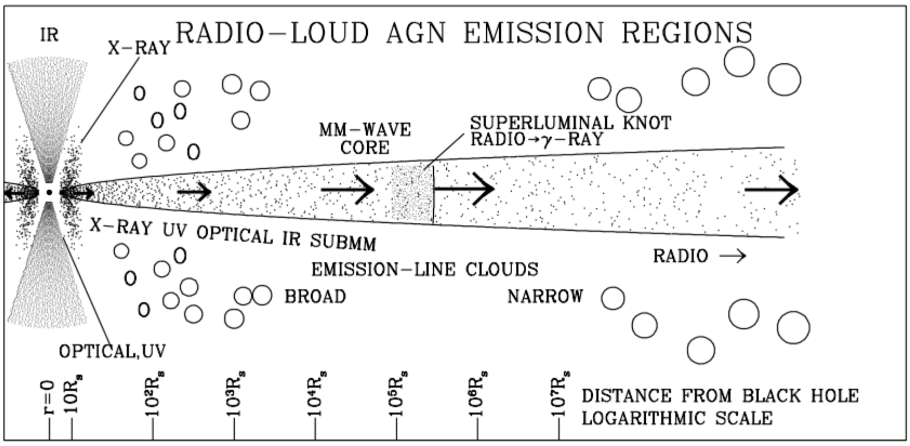

Figure 2.3: [27]. AGN emit thermal radiation from the torus, accretion disc, the BLR and the NRL (IR/Optical/UV/X-ray). The collimated jets in radio-loud AGN emit strongly in the radio and gamma bands and lead to superluminal velocities of jet features being observed for small viewing angles.

2.2.2 Relativistic Effects

Relativistic Beaming

Any emitting object moving at relativistic speeds undergoes a change in emission in the observers frame known as Doppler boosting. This effect is also present in relativistic jets. In this process the relativistic speeds at which photons are travelling cause them to 'catch up' with each other. This leads to an increased flux in the observers frame and the effect is enhanced in jets pointed at small line-of-sight angles.

The luminosity Doppler boost is given by

$$\mathrm{L_{app}} = \mathrm{L_{int}}\delta^n. \tag{2.1}$$

Where $\mathrm{L_{app}}$ is the apparent luminosity and $\mathrm{L_{int}}$ the instrinsic luminosity, and n is dependent on the spectral index and geometry and is typically of value between 2 and 3 [19]. δ is the Doppler factor given by

$$\delta = \frac{1}{\gamma(1 - \beta\cos\theta)} \tag{2.2}$$

where θ is the angle the jet makes with the line of sight of the observer and γ is the Lorentz factor. Equations 2.1 and 2.2 show the dependency of the the apparent luminosity on the viewing angle and on the velocity of the source. A graphic representation of the luminosity Doppler factor as a funcion of speed β is given in Fig. 2.4

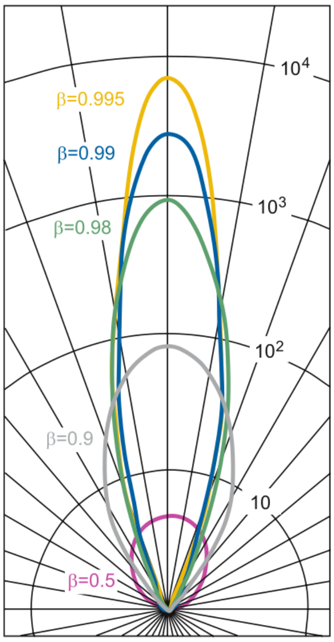

Figure 2.4: [19]. The luminosity Doppler boosting factors δ^n at $n = 3$ for different values of β. In polar coordinates, the radial lines represent 10 degree intervals and the concentric circles are the Doppler factors. Values of β: Red = 0.5, Grey = 0.9, Green = 0.98, Blue = 0.99, Yellow = 0.995.

Lorentz factors range up to at least 45 in the fastest AGN jets [27]. The tendency of blazars to be gamma-loud can be explained through the Doppler beaming phenomenon - they are the sources with small enough viewing angle to produce such luminosity boosting. Gamma-loud blazars are now being detected in TeV surveys and the sensitivy increases in gamma detection will play a huge role in complementing radio observations to enhance our understanding of the most energetic AGN.

Superluminal Motion

Similarly, due to the small viewing angle, features moving in the jet can appear to travel at speeds greater than c. Such behaviour is known as superluminal motion.

Superluminal speeds of up to 50c have been observed for the brightest blazars, with the speed distribution peaking at around 10c [16]. Such observations lead to a relativistic interpretation of the kinematics and emission from AGN jets.

To explain the phenomenon we imagine a source moving at velocity v from P_1 to P_2, separated by a distance $l = v\Delta t$ in time Δt, as shown in Fig. 2.5

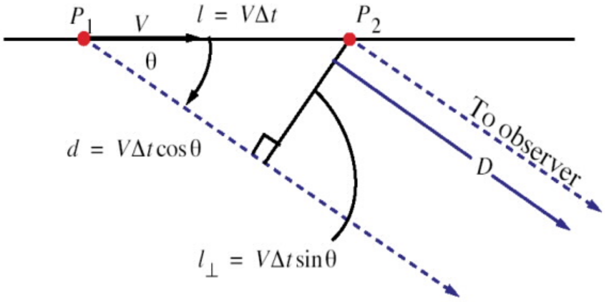

Figure 2.5: [4] A source moving from P_1 to P_2 at an angle θ w.r.t. an observer.

An observer is located at a distance D from P_2, at an angle θ w.r.t. the direction of the source. In time Δt the observer sees the source move a distance $l_\perp = v\Delta t\sin\theta$. For a source located at P_1 and P_2 at times t_1 and t_2 respectively, the difference in time of the light emitted from P_1 and P_2 reaching the observer is given by

$$t_2^{rec} - t_1^{rec} = (t_2 + \frac{\mathrm{D}}{c}) - (t_1 + \frac{\mathrm{D} + v\Delta t\cos\theta}{c}). \tag{2.3}$$

By substituting Δt for $t_2 - t_1$ yields

$$t_2^{rec} - t_1^{rec} = \Delta t(1 - \frac{v}{c}\cos\theta). \tag{2.4}$$

The apparent velocity, v_{app} of the source viewed by the observer is given by

$$v_{\mathrm{app}} = \frac{v\Delta t\sin\theta}{\Delta t(1 - \frac{v}{c}\cos\theta)} = \frac{v\sin\theta}{(1 - \frac{v}{c}\cos\theta)}. \tag{2.5}$$

Defining $\beta_{\mathrm{app}} = v_{\mathrm{app}}/c$ yields

$$\beta_{\mathrm{app}} = \frac{\beta\sin\theta}{1 - \beta\cos\theta}. \tag{2.6}$$

The angle θ which will maximise the apparent velocity can be obtained by differentiating with respect to θ and equating to zero. After rearranging,

$$\frac{\beta\cos\theta - \beta^2}{(1 - \beta\cos\theta)^2} = 0. \tag{2.7}$$

Equation 2.7 holds if $\cos\theta{=}\beta$. To obtain the maximum value of β_{app} we substitute into equation 2.6 and express in terms of β.

$$\beta_{\mathrm{app_{max}}} = \frac{\beta\sqrt{1-\beta^2}}{1-\beta^2} = \frac{\beta}{\sqrt{1-\beta^2}} = \gamma\beta. \tag{2.8}$$

From equation 2.7 we see that $\cos\theta_{\mathrm{max}} = \beta$, and hence β approaches 1 for small line of sight angle θ. Therefore, it is evident from equation 2.8 that β_{app} can have superluminal values for small θ as shown in Fig. 2.6

Superluminal apparent velocites are observed in the object of study of this report and detailed kinematic analsysis of this jet can be found in Section 4.3. Observing the phenomena outlined above relies on the ability to image sources located millions, and even billions, of light years away. To attain such high angular resolution, innovative interferometric techniques must be employed. The basic concepts common to all branches of radio interferometry are discussed in the following section along with the modern practices developed to study AGN.

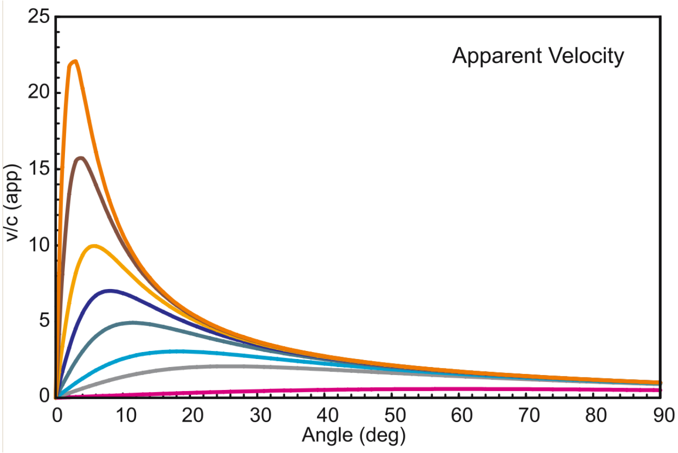

Figure 2.6: [19]. The variation of the apparent velocity β_{app} with line of sight angle for different values of the intrinsic velocity β. The values for β are: Red = 0.5, Grey = 0.9, Light Blue = 0.95, Green = 0.98, Purple = 0.99. Yellow = 0.995, Brown = 0.998, Orange = 0.999.

Chapter 3

Synthesis Imaging and VLBI

3.1 Principles of Radio Interferometry

3.1.1 The Two-Element Interferometer

Through the advancement of radio interferometric techniques, AGN have been imaged with sub-milliarcsecond resolution. To demonstrate the basic principles which form the basis of radio interferometry, we first consider the most highly idealised two-antenna system, before relaxing various conditions in order to attain a more realistic interpretation.

Consider a simple two-element interferometer observing a monochromatic point source **S** in the direction of unit vector $\hat{s}$ as shown in Fig. 3.1

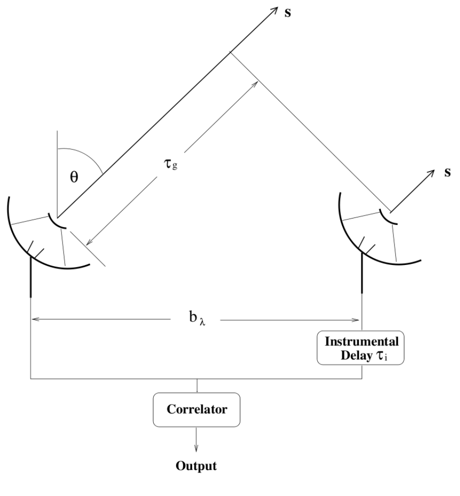

Figure 3.1: [40]. A simple two-antenna system, the delay in the signal arriving at the left antenna is given by the geometrical time delay τ_g. Intrumental time delays can be added to the signal before the correlation process as discussed below.

The antennas are separated by the baseline $\mathbf{b}$. Measured in wavelengths, $\mathbf{b}_\lambda = \mathbf{b}/\lambda$. The unit vector $\hat{s}$ makes an angle θ with the local zenith. The signal arriving at the left antenna (antenna 1) will be delayed by a time $\tau_g = \frac{\mathbf{b}\cdot\hat{\mathbf{s}}}{c}$ known as the geometrical time delay. An intrumental time delay τ_i can be added in order to offset the geometrical time delay, for now however we consider the case with $\tau_i = 0$.

For a monochromatic source at frequency ν, the signal amplitudes received at antennas 1 and 2 will be $x(t) = v_1 \cos(2\pi\nu t)$ and $y(t) = v_2 \cos[2\pi\nu(t - \tau_g)]$ respectively. These signals are cross-correlated by taking their time averaged product. This cross-correlation yields the *cross-power product*, R_{xy}.

$$R_{xy}(\tau_g) = A(\mathbf{s})S\cos(2\pi\nu\tau_g). \tag{3.1}$$

The cross-power product must be proportional to both the effective antenna area $A(\mathbf{s})$ and the source flux S.

By the convolution theorem, the Fourier transform of R_{xy} can be obtained using the Fourier transforms of $x(t)$ and $y(t)$, yielding the *cross-spectrum power density* S_{xy}

$$S_{xy}(\nu) = A(\mathbf{s})S(i2\pi\nu\tau_g). \tag{3.2}$$

Expressing in terms of $\mathbf{b}_\lambda$ yields

$$S_{xy}(\mathbf{s}) = A(\mathbf{s})S(i2\pi\nu \mathrm{b}_\lambda \cdot \mathbf{s}). \tag{3.3}$$

We now consider the effect of the finite bandwidth $\mathcal{B}$ of the receiving device on the interferometer output and relax the (unrealistic) condition of a monochromatic source. A source perpendicular to the antenna baseline would lead to constructive interference occurring at all frequencies. As the source is displaced from the normal, constructive and destructive interference will occur at different positions along the band gap. The result is a fringe pattern with smaller net amplitude known as the *delay beam*.

For an interferometer bandpass given by a square gating function, unity over bandwidth $\mathcal{B}$, with central frequency ν_0 and zero elswhere, the interferometer response becomes

$$P_{xy}(\tau_g) = \int_{\nu_0-\mathcal{B}/2}^{\nu_0+\mathcal{B}/2} A(\nu,\mathbf{s})S(\nu)e^{(-i2\pi\nu\tau_g)}\mathrm{d}\nu. \tag{3.4}$$

P_{xy} is the *cross-spectrum power* and is obtained summing the single-frequency response (eq. 3.2) over the bandpass (the effective area and flux are considered constant over the bandpass). Integrating yields

$$P_{xy}(\nu_0,\tau_g) = A(\nu_0,\mathbf{s})S(\nu_0)\mathcal{B}e^{(-i2\pi\nu_0\tau_g)}\mathrm{sinc}(\mathcal{B}\tau_g). \tag{3.5}$$

From the final term in the above expression, it is evident that when the geometrical time delay τ_g reaches a value comparable to $1/\mathcal{B}$, the delay beam effects are significant and the interferometer response becomes severely attenuated. Thus, as previously mentioned, an artificial delay τ_i must be added to reduce the attenuation effects.

We now remove the point source condition and consider a source of finite size with specific brightness $B_\nu(\mathbf{s})$. We consider the radiation received from a small elemental area of the source, subtending a solid angle $\mathrm{d}^2\Omega$, in the direction

s as shown in Fig. 3.2. The reference direction $\mathbf{s}_0$ is called the *phase tracking centre* and is chosen to be in the direction of maximum antenna gain. It is the position where the intrumental time delay is equal to the geometrical time delay ($\tau_g = \tau_i$). The vector **s** is separated from $\mathbf{s}_0$ by a small vector σ such that $\mathbf{s} = \mathbf{s}_0 + \sigma$.

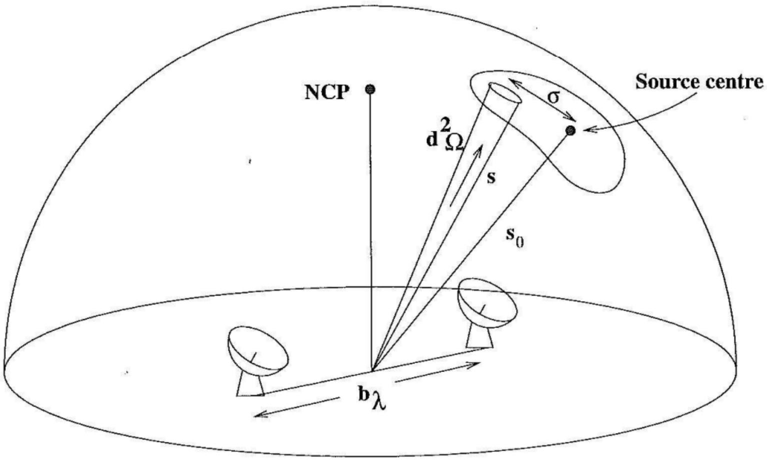

Figure 3.2: [6]. The elemental source area subtending a solid angle $\mathrm{d}^2\Omega$ in direction **s** is displaced from the phase tracking centre $\mathbf{s}_0$ by the small vector σ. NCP is the North Celestial Pole.

Dividing Equation (3.5) by the bandwith $\mathcal{B}$ yields the the cross-spectrum power density S_{xy} (per unit bandwidth). We now consider the source vector **s** in terms of $\mathbf{s}_0$ and σ and include the effect of a non-zero instrumental time delay. S_{xy} can thus be expressed as

$$S_{xy}(\nu_0, \mathbf{s}_0 + \sigma) = A(\mathbf{s}_0 + \sigma) B_{\nu 0}(\mathbf{s}_0 + \sigma) e^{[i2\pi\nu_0(\tau_g - \tau_i)]}\,\mathrm{d}^2\Omega. \tag{3.6}$$

The attenuation term in the above equation has been included as a modification to the effective antenna area $A(\mathbf{s})$. We then define the relative antenna area $\mathcal{A}$, unity in the direction $\mathbf{s}_0$. $\mathcal{A}$ will therefor only depend on σ, and, we can express the cross spectral density in terms of the displacement of the source from the phase tracking centre. This expression can be integrated over the entire radio source to yield the total correlator output.

$$S_{xy}(\nu_0, \sigma) = \int_{4\pi} \mathcal{A}(\sigma) B_{\nu 0}(\sigma) e^{[i2\pi\nu_0(\tau_g - \tau_i)]}\,\mathrm{d}^2\Omega. \tag{3.7}$$

We then make some approximations. First of all we consider the spectrum of the source to be flat. We then assume that the overall source size is small, meaning the difference between the intrumental and geographical time delay, proportional to the length of the vector σ, is small enough to neglect delay beam effects. The frequency of the source can then be defined as the centre frequency, ν_0, defined simply as ν.

By expressing τ_g in terms of σ and $\mathbf{b}_\lambda$:

$$S_{xy}(\mathbf{s}_0) = \int \mathcal{A}(\sigma) B_{\nu 0}(\sigma) e^{i2\pi[\mathbf{b}_\lambda \cdot (\mathbf{s}_0 + \sigma) - \nu\tau_i]}\,\mathrm{d}^2\Omega. \tag{3.8}$$

The intrumental time delay can then be set to cancel out the tracking centre delay. For two elements i and j, separated by baseline $\mathbf{b}_{ij}$ in an array of many antennas, the *complex visibility* V_{ij} is defined as

$$V_{ij} = S_{xy} \text{ when } (\mathrm{b}_{ij} \cdot \mathbf{s}_0) = \nu\tau_i \tag{3.9}$$

Therefore, with this condition, Equation (3.8) becomes

$$V_{ij} = \int \mathcal{A}(\sigma) B_\nu(\sigma) e^{(i2\pi\mathbf{b}_{ij,\lambda}\cdot\sigma)}\, \mathrm{d}^2\Omega. \tag{3.10}$$

Where the baseline vector is expressed in terms of wavelengths. This equation is fundamental in interferometry as it relates the amplitude and phase of the complex visibility V_{ij} to $B_\nu(\sigma)$, the brightness distribution across the sky, through a Fourier transform relationship.

A coordinate system is now needed to describe the relative positions of the baselines in an antenna array. The unit vector $\hat{\mathbf{s}}$, is then defined by its projections l, m, n on the (u, v, w) axes, and the baseline vector $\mathbf{b}_{ij,\lambda}$ is described by its (u, v, w) coordinates, which are expressed in wavelengths (spatial frequency).

The vector $\mathbf{s}_0$ is taken to be in the w direction, with the u, v plane orthogal to this vector. The offset vector σ will therefor be parallel to the u, v plane as shown in Fig. 3.3

To express the complex visibility in the u, v plane we take $w = 0$ (perpendicular to plane), and express the the elemental solid angle $\mathrm{d}^2\Omega$ in terms of the direction cosines l, m, n. Integrated over the whole source, Equation (3.10) becomes

$$V_{ij} = \int_{4\pi} \mathcal{A}(l, m) B_\mu(l, m) e^{[i2\pi(ul+vm)]} \frac{\mathrm{d}l\, \mathrm{d}m}{\sqrt{1 - l^2 - m^2}}. \tag{3.11}$$

It can then be recognised that Equation (3.11) expresses V_{ij} as the integral Fourier transform of $\mathcal{A}(l, m)B_\mu(l, m)/\sqrt{1 - l^2 - m^2}$.

Since the offset angle σ is small, it is useful to replace the direction cosines l and m by the rectilinear coordinates x and y. We take x to be parallel to u, and (x,y) are then the angular offset coordinates. Since $\sqrt{1 - l^2 - m^2}$ in Equation (3.11) represents the projection of $\mathbf{s}$ onto w (equal to $\cos\theta$) we can allow this to equal unity in the small angle approximation (σ angle is small). This yields Equation (3.12) and from it we see that through measuring the phase and amplitude of the complex visibiitly, we obtain the Fourier transform of the source brightness distribution, measured in the celestial angular coordinates x and y, for a partucular value of spatial frequency, given by the baseline vector projected onto the (u, v) plane.

$$V(u, v) \approx \mathcal{A} \int B(x, y) e^{[i2\pi(ux+vy)]}\, \mathrm{d}x\, \mathrm{d}y. \tag{3.12}$$

By making multiple observations of phase and amplitude with different baselines (different spatial frequencies), the Fourier transform of the brighness distribution can be sampled across the whole source, building up (u, v) *plane coverage*. From this, the real brighntess distribution of the source can be obtained through methods described in the following section.

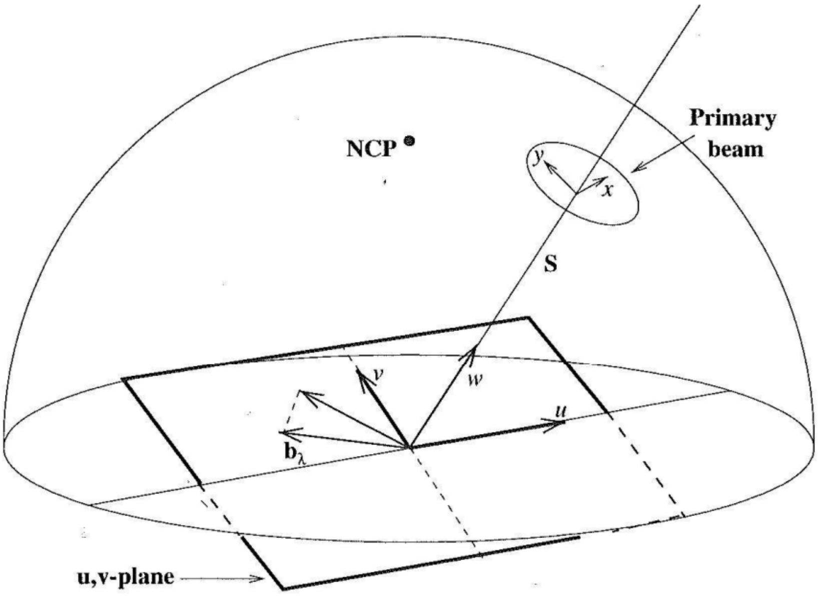

Figure 3.3: [6]. The (u, v) plane is perpendicular to the phase tracking centre vector $\mathbf{s}_0$, in the direction w. The offset angle σ is expressed in terms of the rectilinear coordinates x, y on the celestial sphere.

3.1.2 Aperture Synthesis

The extent to which a map of brighntess distribution reflects the true emission of a source dependent on the (u, v) plane coverage. An antenna array is able to build up this coverage through the many combinations of antenna pairs. Additionally, antenna arrays such as the Very Large Array[1] and MERLIN[2] have moveable antennas, further increasing the number of possible baselines available. In VLBI, the antennas are positioned at arbitrary distances from each other and the baselines are of much greater lengths that in localised arrays. Through VLBI much greater angular resolution can be achieved but the positions of the antennas make it harder to produce a map of source brighness distribution from the (u, v) coverage (see Section 3.2.2).

Earth rotation synthesis, devised by Sir Martin Ryle in 1962 (Nobel Prize 1974), exploits the changing orientation of baselines with respect to the source as the earth rotates in order to further increase the (u, v) plane coverage. In a given array of N radio telescopes, there are $N(N-1)/2$ ways of pairing these telescopes to act as a two-element interferometer. Thus, at any one time, the visibility funcion $V_{ij}(u, v)$ can be sampled at $N(N-1)/2$ points, an example of the instantaneous, or 'snapshot', (u, v) plane support is shown in Fig. 3.4

---

[1] The Very Large Array (1976) is an antenna array consisting of 27 radio telescopes of 25m diameter arranged in 'Y' shape. It has a maximum baseline of around 35km and is situated in Socorro, New Mexico.

[2] MERLIN is the Multi-Element Radio-Linked Interferometer Network consisting of 7 antennas distributed across England with a maximum baseline of around 200km.

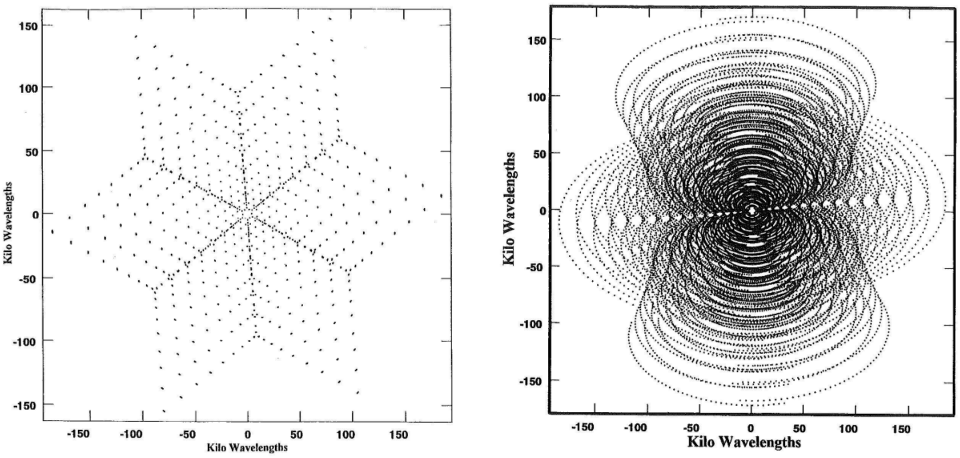

Figure 3.4: [6]. **Left:** The 'snapshot' coverage of the 27-antenna VLA for an observation at the zenith. **Right:** The (u, v) coverage for a earth-rotation tracking observation lasting 8 hours for a source at δ=30°. There will always be a gap at the origin of a (u, v) plot as all baselines have finite length.

(left). As the earth rotates, the baseline will sweep out an ellipse is the (u, v) plane. The source position will determine the axial ratios of the ellipses, with high declination sources leading to more circular traces and sources near the celestial equator leading thinner traces, with δ=0 sources showing straight lines on a (u, v) plot. Tracking observations, as shown in Fig. 3.4 (left), lead to high (u, v) coverage. Since each baseline has length but not direction, each point will be reflected about the origin.

Aperture synthesis techniques are employed extensively in experiments at the forefront radio astronomy. Experiments such as the Square Kilometre Array (SKA) and the Atacama Large Millimeter Array (ALMA), in their design and construction phase respectively, mark a new era in radio astronomy. SKA, which is due to be fully operational by 2024, will consist of radio antennas spread over a distance of 3000 km across Australia, South Africa and New Zealand linked to a central correlating facility. Through aperture synthesis techniques, the SKA antennas will combine to produce resolution equivalent to a single antenna with an effective area of 1 square kilometre. ALMA is due to be completed in late 2012 and will consist of 66 12-m and 7-m radio telescopes located in the Atacama desert in northern Chile. These experiments, along with their precursors and pathfinders, have been dubbed the 'golden age of radio astronomy' and will exploit aperture synthesis methods to look deeper into our universe than ever before.

3.2 Imaging and Calibration

3.2.1 Data Reduction and Calibration

In contrast with classical astronomy, radio astronomy does not register optical images in a chemical film or in a couple charge device. Radio telescopes register the voltage produced by the electromagnetic radiation exciting a dipole, the receiver. Radio interferometers register the correlation function of the voltages registered in several telescopes, as shown in previous section. To convert these voltages and correlation coefficients to an image of the radio source brightness distribution in the sky, calibration is needed. The final image will be obtained by Fourier deconvolution, as will be shown in this section.

Calibration sources are required in order to keep track of any variations in factors which affect the visibilities measured by the antenna arrays. Both flux calibrators and phase calibrators are required and these sources should ideally be point-like and close to the target source. Phase calibrators must be stable in position and close to the object to be mapped as frequent reference must be made to them. The flux of ideal flux calibrators should be able to be determined very accurately and should be subject to very small variation over time. They should also be compact enough not to be resolved by the interferometer baselines. These requirements are often hard to meet since small sources tend to have variable flux.

Data from the calibrator sources is used in order to identify any ‘bad’ visibility data, and the accuracy of the measured visibilities can be optimized through analytical techniques utilizing the calibrator data. Closure relations can be used in order to remove phase and amplitude inaccuracies due to atmospheric and instrument-induced effects. For a set of three antennas i, j, k, the total fringe phase can be expressed as a sum of the fringe phases of the antenna pairs.

$$\phi_{ijk} = \phi_{ij} + \phi_{jk} + \phi_{ki}. \tag{3.13}$$

ϕ_{ijk} will be independent of phase shifts brought about by the atmosphere or instruments and thus closure phases of different antenna sets can be combined algebraically in order to calculate the phase shifts induced in other individual antennas. These will of course all be relative to a single chosen antenna phase correction.

Similarly, the amplitude closure relation (3.14) can be used to correct for fringe amplitude errors.

$$A_{ijkl} = \frac{|V_{ij}|V_{kl}|}{|V_{ik}||V_{jl}|}. \tag{3.14}$$

Accurate data calibration requires extensive computation and there exist various programs, such as the Astronomical Image Processing System (AIPS)[3], which automates parts of the data-reduction process, although input from an experienced observed is required to obtain best results.

3.2.2 Synthesis Imaging

The Dirty Map

The task of producing a map of brightness distribution from u, v-plane coverage relies heavily on Fourier methods. From Equation (3.12) we see that the complex visibility in the (u, v) plane is related to the source brightness distribution, measured through the offset angles x, y relative to the phase tracking centre, through a Fourier transform relationship.

$$V(u, v) \xrightleftharpoons{FT} B(x, y) \tag{3.15}$$

---

[3] www.aips.nrao.edu/

If $V(u,v)$ were known continously across the source, the true sky brightness distribution could be built up by performing inverse Fourier transforms. However, radio interferometric techniques allow only the *sampled* visibility distribution $S(u,v)V(u,v)$ (Equation 3.16) to be measured, and, due to the inevitable gaps in the (u,v) coverage, the inverse Fourier transform of this sampled visibility will produce an inferior image known as the *dirty map*, B^D (Equation 3.17)

$$S(u,v)V(u,v) = \sum_k (u_k, v_k)V(u,v) \tag{3.16}$$

$$\mathcal{F}[B^D(x,y)] = [S(u,v)V(u,v)]. \tag{3.17}$$

From the convolution theorem it can be shown that

$$B^D(x,y) = \mathcal{F}^{-1}[S(u,v)] \otimes B(x,y) = s^D(x,y) \otimes B(x,y) \tag{3.18}$$

The dirty map is therefor equal to the true brightness $B(x,y)$ convolved with the point spread function $s^D(x,y)$ known as the *dirty beam*. In order to produce the brightness map (*clean map*), the $B(x,y)$ must be deconvolved from the dirty beam $s^D(x,y)$. The next section deals with this deconvolution process.

In order to produce the dirty map, the (u,v) data must first be gridded so that a Fast Fourier Transform (FFT) can be carried out computationally. The pixel size must be set so as not to exclude any sampled visibility information, in practice it is usally set so that the main lobe of the dirty beam in 3 to 5 pixels wide [41].

The exact shape of the dirty beam also depends on the weighting function $W(u,v)$ which is included in the gridding process.

$$s^D = \mathcal{F}^{-1}[W(u,v)S(u,v)]. \tag{3.19}$$

The weighting functions often applied in practice include 'Natural' weighting and 'Uniform' weighting

'Natural' weighting

Weights all data points equally - $W(u,v) = 1/\sigma^2$ where $\sigma(u,v)$ is the noise variance of the (u,v) sample. It effectively minimises the noise in the image and maximises the signal to noise ratio, a limiting factor in the achievable resolution.

'Uniform' weighting

Gives less weight to densely populated areas of the map - $W(u,v) = 1/\sigma$. It gives more weight to long baselines hence decreases the size of the beam and increases the resolution, whilst increasing the noise of the map.

In practice hybrid versions of both the above weighting functions can be created by varying the power on the noise variance which scales the gridding weights.

The CLEAN Algorithm

An effective way to deconvolve the source brightness from the dirty map was devised by Jan Högbom in 1974 [13]. The main steps in the process are outlined below.

1. The brightest point on the dirty map is located and from it is subtracted the dirty beam response to a point source, including the full sidelobe pattern, centred on that position. The loop gain, γ, is defined as the ratio of the maximum amplitude of the subtracted point source to the amplitude of the corresponding dirty map point.

2. The point source component subtracted is recorded on a different map as a delta function with conserved position and amplitude. This map is called the *cleaned map* and is made up of *clean components*. The *residual map* is the dirty map minus the subtracted clean components.

3. Clean components are removed from the dirty map until no bright features can be distinguished and the residual map resembles noise.

4. In the cleaned map, the delta functions are then replaced with *clean beam* functions of same amplitude. The clean beam is the response of a point source without sidelobes but with same full width half max (FWHM) as the dirty beam.

5. The noise from the residual map is added to the cleaned map.

The iteration process in Step 3 should be carried out until the rms level of residual intensity is comparable to the highest peak, or until a significant amount of negative cleaned components are removed.

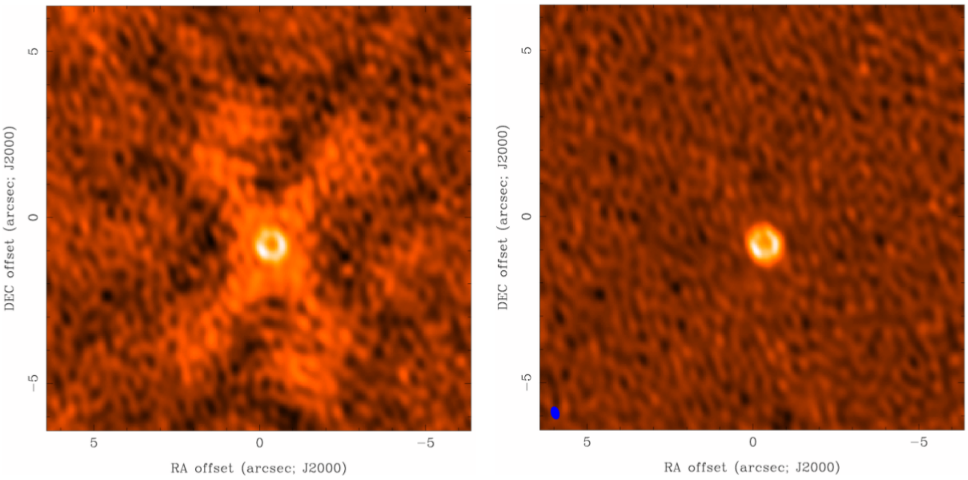

Figure 3.5: [41]. A brightness map before and after the implementation of the CLEAN process. The dirty beam (left) shows the source surrounded by the sidelobes of a point spread function. These have been removed through the CLEAN algorithm to yield the 'cleaned' map (right).

Model Fitting

The implementation of the CLEAN algorithm allows high quality maps of the brightness distribution of the source in the sky to be obtained by modeling the visibility data using many Kronecker delta functions. These functions are easily handled computationally but other models can be chosen depending on the aims of the astronomer. In order to quantitively analyse the changes in position and flux of individual features of the source over time, gaussian model components are particularly useful due to the fact they are always positive and vary smoothly with angle. The stages involved in producing a map through gaussian model fitting are stated explicitly in Section 4.2.2.

Once an accurate model has been created, the residual map should resemble noise as in the CLEAN process. This usually involves fitting several individual gaussian components to bright regions on the dirty map. These components will have specific values of flux and position amongst other attributes depending on the feature they model.

The goodness of fit of the model is calcualed in a least squares fit method described by the reduced χ^2 function which sums the difference between the squares of the model and of the data and divides by the number of degrees of freedom of the model component parameters across the map. In order to minimise the reduced χ^2, various parameters of the model can be varied (position, axial ratio, etc.). Depending on the requirements of the astronomer, these parameters can be set to vary in order to achieve the minimum χ^2 or can be kept constant to facilitate comparison between different models.

The model fitting method allows the kinematic analysis of the object of study in this report to be carried out. It is especially valuable as the model components used in one epoch can be saved and applied to other epochs in order to monitor the properties of individual features in time.

Self-Calibration

Self-calibration can be used throughout the deconvolution process in order to reduce any residual phase and amplitude errors. The map of source brightness produced through the above methods cannot represent the true source brightness due to inevitable phase and amplitude calibration errors and noise. From this model however, since the baseline vectors are known, one can determine what visibilities would have been measured originally to produce this map. These visibilities will also of course be different from the visibilities originally observed, and, taking into consideration the weighting of the modeled visibilities, the two can be compared.

$$\sum_k \sum_{i,j} W_{ij}(t_k)|{V_{ij}}^{cal} - g_i(t_k){g_j}^*(t_k){V_{ij}}^{mod}(t_k)|^2 \rightarrow 0 \tag{3.20}$$

This represents Schwab's method in which the complex gains g_i added to the modeled visibilites are varied in order to minimize the differences between the two visibilites in a least-squares sense. W_{ij} is the weighting function applied to the interferometer pairs at time t_k.

The 'cleaned' image of the true brightness distributtion of the source is usually obtained after implementing several loops of the CLEAN process and self-calibration. The process of using both the CLEAN algorithm and self-calibration to produce a map is known as *hybrid imaging*.

Images of the object of study of this report created using the hybrid imaging technique are shown in Section 4.2. The visibility data was also modeled using gaussian model compoenents which allowed the kinematic analysis of the jet features to be carried out (Section 4.3).

3.3 Very Long Baseline Interferometry

3.3.1 Method

The antenna arrays used Very Long Baseline Interferometry consist of individual radio telescopes located in arbitrary positions, spanning countries and continents. The baselines can be made even larger by incuding an antenna positioned on an orbiting satellite. Unlike arrays such as the VLA, the elements are not usually connected by transmission lines in order to cross-correlate signals[4]. The baselines in VLBI are around 2 orders of magnitude larger than 'hard-wired' arrays such as the VLA and MERLIN and therefore, utilise a different technique which involves storing data on devices (previously magnetic tape, now usually hard disc drives) before transporting it to a supercomputer known as a *correlator* to carry the cross-correlation. The timing and frequency standards must be extremely precise and the recording and reading out of the signal must preserve this timing information.

VLBI can provide milliarcsecond resolution, corresponding to parsecs at cosmological distances and operates at wavelengths from 3mm up to 1m. The upper wavelength limit is set by the ionospheric dispersion effects which start to become significant above metre-wavelengths. The highest resolution is achieved at shortest wavelengths but at sub-millimetre wavelenghts, observations are disturbed by water vapour, oxygen, and carbon-dioxide molecules. In practice, wavelenghts of 7mm to 18cm are most commonly used [31].

The signals received at the individual antennas are first amplified by a low-noise amplifier. The next step is to convert the original frequency ν_o into an intermediate frequency ν_i, which is facilitates the transmission of the signal. This is done by combining it with a local oscillator frequency ν_{lo}.

$$\nu_i = \nu_o \pm \nu_{lo} \tag{3.21}$$

The local oscillator frequencies added at the individual antennas must be equal across the whole array and need to be set to a very high degree of accuracy. The frequency standard is set by a hydrogen maser which is also used to generate time pulses in order to include the timing information in the signal. The signal is then recorded onto a hard disc and transported to the central facility where the cross correlation is carried out. When the information is read out, the necessary instrumental time delays are added and the signal is cross correlated.

3.3.2 Current Surveys

The first VLBI observations were performed in the early 1970's and since then both astronomical and geodetic aims have led to numerous VLBI surveys being comissioned.

VLBI has been used to set the International Celestial Reference Frame (see [25]) and to monitor many geophysical parameters such as the motions of tectonic plates and the length of the day.

Arrays such as the Australian Long Baseline Array (LBA) and the European VLBI Network (EVN) consist of individual radio antennas, built separately to

---

[4] Recently some VLBI networks have used fibre optic cables to transfer data in real-time, known as eVLBI. See next section

different specifications, which carry out coordinated VLBI observations at certain times throughout the year. The TANAMI array (see below), which extends the LBA, consists of 10 radio telescopes located across Australia and South Africa. The EVN is made up of 18 telescopes with 5 non-Europen telescopes located in China, South Africa and Puerto Rico, the largest being the 100m diameter Effelsberg radio antenna in Germany. The correlation of EVN signals takes place in Dwingeloo in the Netherlands. Both the LBA and the EVN are now developing eVLBI programs working towards the transmission of recorded signals to a central supercomputer in real-time through fibre optic cables. eVLBI requires advanced data transfer techniques and the eEVN has been recognised as an official SKA pathfinder in devolping the high rate data transport and processing methods.

VLBI baseline lenghts were further extended through the VLBI Space Observatory Programme (VSOP) which positioned an 8-m radio telescope on board the $HALCA$ satellite in elliptical Earth orbit in 1997.

The only array dedicated to VLBI Observations is the Very Long Basline Array (VLBA) which consists of 10 identical 25m telescopes located across North America (see Fig. 3.6). The longest VLBA baseline is of 8611km between St. Croix on the Virgin Islands and Mauna Kea in Hawaii. The VLBA can achieve a maximum angular resolution of 0.17 mas at a wavelength of 7mm [40]. The VLBA correlator is located in Socorro, New Mexico.

Along with imaging AGN, VLBI is used to observe more compact sources such as radio supernovae, pulsars and X-ray binary stars.

In the last decade, several projects have been designed to monitor AGN parellel to gamma observations from the Large Area Telescope on board the $Fermi$ satellite launched in 2008. The Boston University Blazar Program[5] has been imaging AGN at 43 GHz since 2007 using the VLBA. The TANAMI project[6] (Tracking AGN with Austral Milliarcsecond Interferometry) observes at 8.4 GHz and 22 GHz using the LBA and other additional telescopes in South Africa and has been operating since 2008.

The data used in this report was observed in the MOJAVE Survey (Monitoring Of Jets in Active galactic nuclei with VLBI Experiments). The VLBA 2cm Survey started in 1994 and was renamed 'MOJAVE' in 2002. It observes over 300 sources above $\delta = -30°$ at 15 GHz using the VLBA. The monitoring is continous and the MOJAVE database is maintained by [23].

---

[5] www.bu.edu/blazars/research.html

[6] http://pulsar.sternwarte.uni-erlangen.de/tanami/

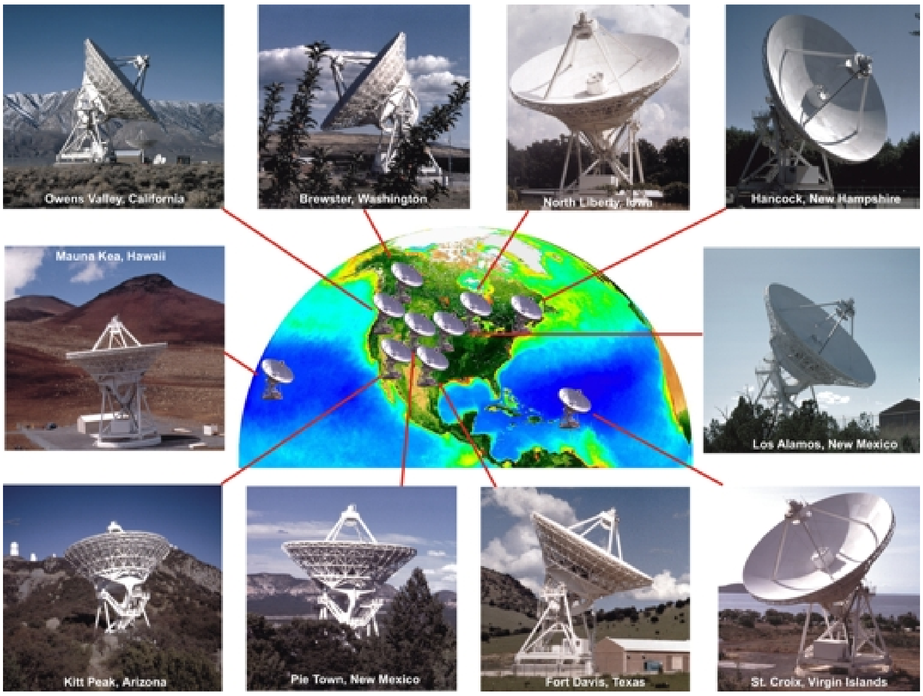

Figure 3.6: [28]. The positions of the VLBA antennas spanning North America.

Chapter 4

Method and Results

4.1 Object of Study

When choosing a suitable source to use as the object of study, various considerations were taken into account. Firstly, it was deemed appropriate that the source be under observation at gamma wavelengths also, therefore the preliminary list of possible candidates was taken as the source list in [31].

These sources are monitored by MOJAVE at 2 cm wavelengths, along with the Large Area Telescope (LAT), the principal scientific instrument on the *Fermi* Gamma Ray Space Telescope launched in June 2008.

Of the catalogued sources in [31], a shortlist was made to include only those sources with a well defined 'one-sided jet' kpc-scale morphology. The decision was then taken to discard any sources which had already been subject to detailed kinematic analysis or that were currently being analysed within the Radio Astronomy department in the University of Valencia. On this basis, the Blazar B1551+130, (or J1553+1256) was chosen as the object of study.

As detailed in the MOJAVE data archive, B1551+130 is estimated be of redshift $z = 1.308$, corresponding to a luminosity distance of 9280 Mpc[1]. It is a flat spectrum radio quasar (FSRQ) observed in 6 epochs in the MOJAVE 2cm Survey, the first in June 2009 and the most recent in late April 2012 (see Tab. 4.1).

The radio spectrum of the object of study is shown in Fig. 4.1. The self-absorbed synctron radiation from the core and syncrotron emission from the jet combine to configure this spectral shape. An optical image of the source is also shown in 4.2.

4.2 Images

4.2.1 Hybrid Mapping

The image deconvolution in this project was carried out in the program DIFMAP[2]. DIFMAP was written by Martin Shepherd at Caltech and allows brightness maps to be created through both hybrid mapping and gaussian model fitting along

---

[1] assuming $H_0 = 71$ kms^{-1}Mpc^{-1}, $\Omega_\Lambda = 0.73$, $\Omega_m = 0.27$

[2] ftp://ftp.astro.caltech.edu/pub/difmap/difmap.html

Epoch	**Observation Date**	**Year Fraction**
1	03/06/2009	2009.42
2	19/08/2009	2009.63
3	10/03/2010	2010.19
4	27/09/2010	2010.74
5	11/04/2011	2011.28
6	29/04/2012	2012.33

Table 4.1: The dates of observation of the MOJAVE data for each Epoch available.

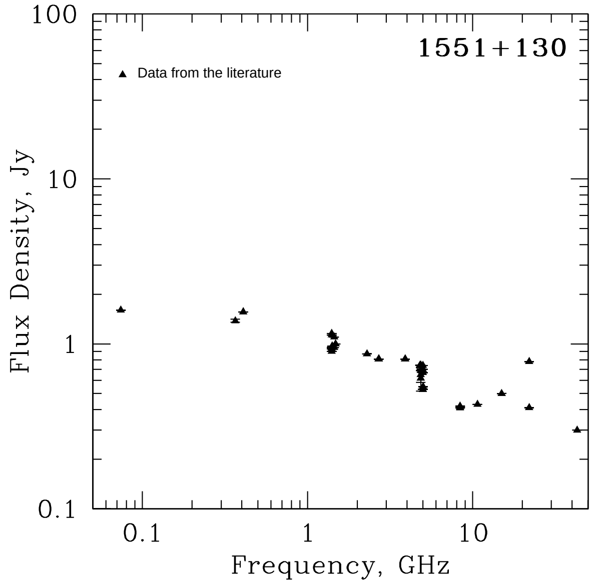

Figure 4.1: [23]. The radio spectrum of B1551+130 from the MOJAVE Database. The presence of high-frequency radio emission shows that the source is dominated by the mm-wave core. Objects with a spectral index steeper than -0.7 are classified as FSRQs.

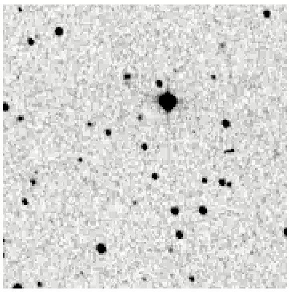

Figure 4.2: [8]. An optical image of B1551+130 taken with the 48-inch (1.2m) Schmidt telescope at the Caltech Palomar Observatory

with many other feautures used to analyse VLBI continuum data. A description of the main features and functions of DIFMAP can be found in [34].

The data for the source taken from the MOJAVE database was in the form of a UVFITS file which was read into difmap. For each epoch the same procedure was followed to create the hybrid maps.

First of all, the pixel size was chosen. For this source a map of 512 pixels with a pixel size of 0.1 milliarcsecond was suffiecntly small. DIFMAP warns the user if an innapropriate pixel size is set and recommends an appropriate value.

Natural weighting was chosen for the gridding to allow effective comparison of the maps produced with those of the source in the MOJAVE data archive which use natural weighting.

The brightest area on the dirty map was highlighted by placing a rectangular 'window' over it. This window tells DIFMAP in which area of the map to carry out the desired command. The CLEAN algorithm was then run by simply inputting the CLEAN command on the user interface. The loop gain and the number of iterations are also specified in this command. During the hybrid mapping process, a CLEAN-selfcalibration 'loop' was often implemented. This command tells DIFMAP to carry out the CLEAN process (with specified loop gain and iteration number) and then self calibrate the visibility data before implementing the CLEAN algorithm and repeating this process a user-defined number of times. The typical values of loop gain specified in the CLEAN command was 0.1 with 200 iterations.

The CLEAN command returns the value of total flux cleaned from the map every 50 iterations. The selfcalibration, or SELFCAL, command returns the rms difference between the model and the data before and after the self-calibration. Both these values assist the user in deciding when the CLEAN-SELFCAL process has been carried out a sufficiently

After every CLEAN-SELFCAL loop, the residual map is viewed by inputting the MAPPLOT command. The brightest areas in the map are then identified and highlighted with a 'window' and the CLEAN-SELFCAL process is repeated.

It is also important to keep an eye on the clean components which have been subtracted from the model. When the user specifies, these clean components will appear on the map as points with different colours for positive and negative components. A presence of a significant amount of negative components may indicate the model has been cleaned sufficiently. The extent to which the model fits the visibility data can also be visualised using the RADPLOT and PROJPLOT commands. These will show both original visibility data and the model in different colours and plot the visibility amplitudes as a function (u, v) plane radius and (u, v) plane projected distance (with variable angle) respectively.

When the residual map resembles noise and there are no prominent bright features on the map, the clean map should be complete. As a final enhancement, the CLEAN command was run over the whole map, with a high number of iterations and small loop gain (1000,0.01) in order to reduce the overall noise of the map.

The contour levels on the hybrid maps were set at a value which showed the map in sufficient detail, whilst minimising the apparent noise. The contour levels increase on a logarithmic scale and were set be of base 2. The minimum value was set at 0.2% hence the contour levels were 0.2%, 0.4%,0.8%...51.2% of the map peak (measured in Jy/beam). DIFMAP also adds in one negative contour of the magnitude of the minimum positive value, i.e –0.2%. The values

Epoch	Map Peak (Jy/beam)	Beam FWHM (mas)	Total Flux Imaged (Jy)
1	0.407	1.08 × 0.57 at $-1.98°$	0.664
2	0.443	1.09 × 0.52 at $-5.95°$	0.721
3	0.340	1.13 × 0.51 at $-8.66°$	0.600
4	0.563	1.18 × 0.54 at $-4.70°$	0.856
5	0.528	1.04 × 0.48 at $-3.37°$	0.802
6	0.488	1.27 × 0.60 at $-9.66°$	0.803

Table 4.2: Properties of the hybrid maps for each epoch. The Map Peak is the brightness flux at the point of highest intensity on the map. The Beam FWHM is the size of the clean beam which was used in the deconvolution to produce the clean map given with the position angle of the major axis of the ellipse.

of peak intensity and the FWHM of the clean beam are shown in Tab. 4.2. The hybrid maps are shown in Fig. 4.3.

The images show the source with a one-sided jet, extending from the core region. The core at the base of the jet is the brightest area, with the highest flux measured in Epoch 4 (0.536 Jy/beam). The part of the jet extending to around 5 mas declination has a slight 'backwards 'S" morphology. Between around 5 mas and 7 mas declination the jet shows an area of more diffuse intensity with no clear peaks. The intensity in this region is lowest in Epochs 4 and 5 before increasing again in Epoch 6. At the extremity of the jet, a wider 'lobe' region is evident, weakest in Epoch 5.

4.2.2 Gaussian Model Fitting

The MODELFIT command in DIFMAP allows intensity models to be fitted to visibility data. The first step is to identify the brightest area on the dirty map and 'cover' it with a gaussian model component of appropriate size and shape. In this project, the models were chosen to be circular gaussians. This was decided in order to allow effective comparison between the model components over the epochs. Although elliptical gaussians often provide a better fit to the data, they are unsuitable when tracking the motion of individial components as their axial ratio will change in order to 'cover' areas of high flux with no distinct peak. This results them often degenerating into straight lines and makes the changes in flux and position of individual features hard to model.

After each MODELFIT command the residual map will show new areas of higher intensity and new components are fitted in order to model the data. When the residual maps resembles noise and no bright features are evident, the model is complete.

The MODELFIT command subtracts the model specified by the user from the visibility data. It will adjust the parameters of the model after each iteration in order to the reduce χ^2 value. The model component parameters kept variable during the model fitting process were: flux, postion (x and y), and FWHM. The axial ratio was kept constant at 1 (circular components).

After each MODELFIT iteration, the value of the reduced χ^2, along with the parameter values, are returned. The aim of the model is to achieve the lowest possible χ^2 value whilst maintaining 'healthy' component parameters. After each new component is added, the the MODELFIT command is entered along with

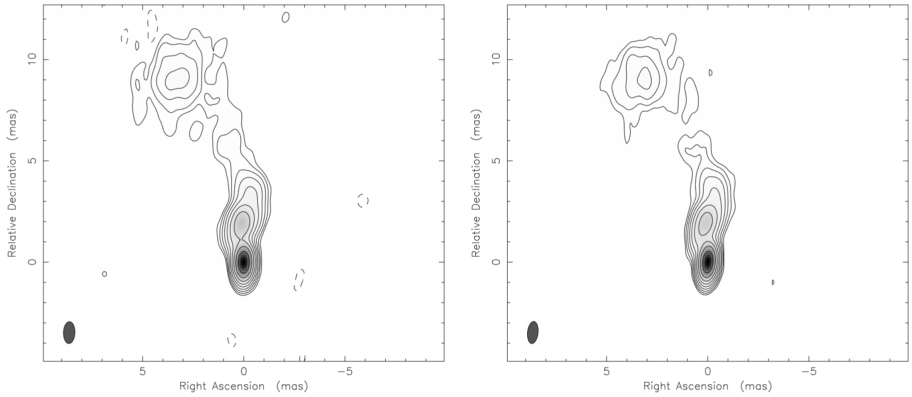

(a) 03/06/2009 (b) 19/08/2009

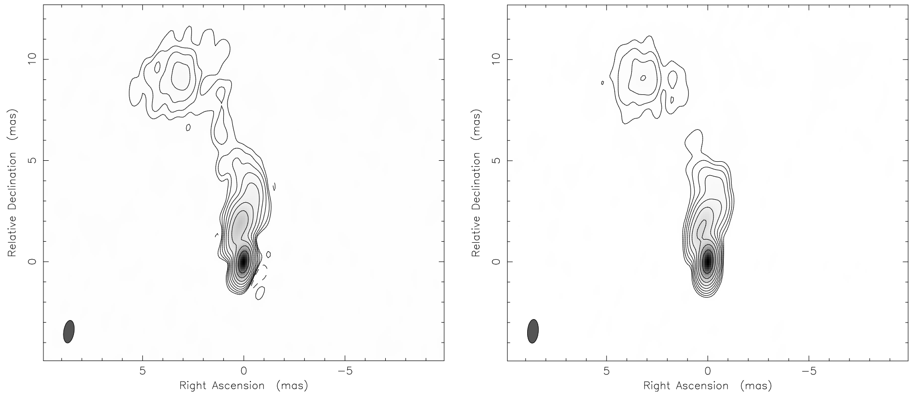

(c) 10/03/2010 (d) 27/09/2010

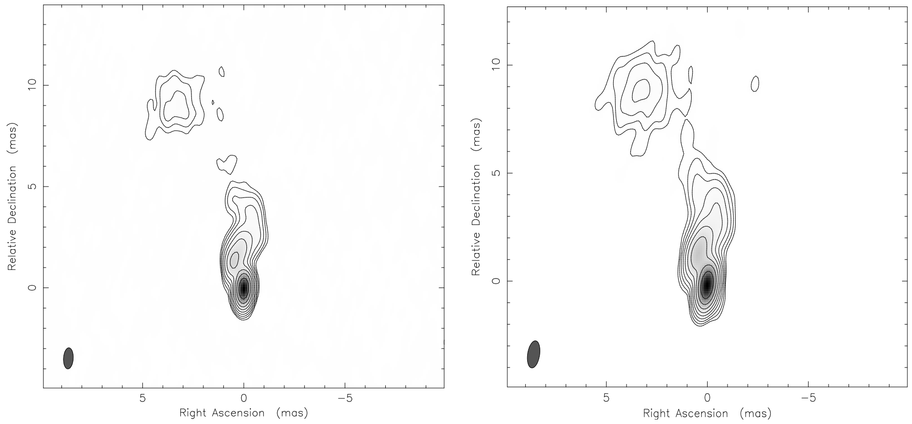

(e) 11/04/2011 (f) 29/04/2012

Figure 4.3: Hybrid maps realised with DIFMAP for Epochs 1-6 ((a)-((f)). The contour lines range from -0.2% to 51.2% of the map peak. Darker areas show areas of higher intensity.

the desired number of iterations (usually between 10 and 20). As the component parameter values are returned over the iterations, it is important to keep an eye on the parameter values of the new components. Unrealistic component parameters such as the component turning negative, inflating to large width, or its position changing greatly from the area it was placed, are indications of innapropriate model components. Such components can be deleted from the model using EDMOD command which displays the components and their parameters and allows them to be edited.

If, after a number of MODELFIT iterations, the reduced χ^2 stays constant, i.e converges on a value, the model components have been fitted appropriately and the dirty map is then shown to identify bright areas on which to fit a new component. Each component should be fitted one at a time prior to the MODELFIT, and, before a new component is identified from the dirty map, a phase self-calibration should be performed through SELFCAL.

The appropriate values for the reduced χ^2 are $\simeq$1. During the model fitting process the values obtained ranged between 1.02 and 1.08, which were deemed appropriate.

After a model for a map was completed, the model components were saved in order to be used for the next epoch using the WMOD and RMOD commands (write model, read model). This saved time in having to input the model components for each epoch from scratch and also allowed the componets to be monitored across the epochs. When the model is loaded into the new map, the MODELFIT command is run until the reduced χ^2 converges. That model is then saved and used for the subsequent epoch and so on until the final epoch model has been made.

When adding the model components, one has to find the number of components which accurately model the visibility data, such that any more components which *could* be added are deemed unnecessary. For the object of study, eight model components were shown to provide an adequate model of the visibility data. Component 7 (see Fig. 4.5) was a somewhat difficult component. It was the last component to be added to the model and was made to cover an area of increased brightness evident on the residual map after the previous 7 components had been added. In the first epoch, through adding this component the χ^2 value decreased and the component remained stable in position and size. When this model was loaded into the next epoch however, running the MODELFIT command resulted in it increasing to an unrealistic width. When the component was removed from this epoch the χ^2 value increased and it was evident from the residual map that the model needed a component to cover that area. The same was true across the other epochs whereby the model 'wanted' the component but it remained relatively stable in position but not in size. The decision was then taken to fix the width of the component to the value that yielded the smallest χ^2 value in the *first* epoch, and then carry it through to the other epochs along with the other seven components. The area on the map which is represented by this component has a very diffuse flux, therefore when MODELFIT changed the parameters of the component to reduce the χ^2 value it found that it could do so by increasing the width of the component to cover more of the diffuse area as it had no strong peak. However, analysis of such diffuse features is not the object of this report, therefor the component was fixed to create a better model but is regarded as *non-robust*.

The weighting set in the modelfitting process was kept as the default 'Uniform' weighting. Since the antennas of the VLBA are identical, the signal to noise ratio will be constant across the array and therefor uniform weighting was deemed appropriate.

When the models for all 6 epochs were completed, the values of flux, position and FWHM of the model component were transferred to a spreadsheet package. The postions of the components are returned in polar coordinates in DIFMAP and these were converted to (x, y) coordiantes in the spreadsheet. The source data loaded from the UVFITS file into DIFMAP had been calibrated to set the core of the jet as the origin of the map. However, due to small fluctuations of the core position over time as described in [31], it is important to correct the component positions for each epoch to ensure they are measured with respect to the brightest feature on the map, the core (Component 1). This was done by calculating the x and y coordinates of Component 1 and adding in small corrections to them to move them to the origin. These same corrections were added to all the components in the epoch and the same procedure was followed in the other epochs. Subsequently, the radial distance from the origin was calculated from the corrected x and y values. Tab. 4.3 shows the component parameters read out from MODELFIT process DIFMAP. The corrected x and y values are also shown along with the corrected radius.

The maps produced through MODELFIT are shown in Fig. 4.4. The circular gaussian components are shown in red. In order for the model components to be seen more easily in these maps, some visual aspects were changed with respect to the hybrid maps in Fig 4.3. Firstly the contour levels were changed. The contour levels on the MODELFIT maps increment on a logarithmic scale to the base 4, with minumum value 0.5% (-0.5%, 0.5%, 2%, 4%...32%) of the map peak. Additionally, the grayscale shading relative to intensity was removed so that there was no dark area in the core of the jet. Note the FWHM of the model components tend to increase along the jet from the core to the lobe. The components represent 'knots' of high radio intensity along the jet. Knots closer to the core will have a more highly peaked intensity as the features will 'spread out' as they move further away from the core. The component with the smallest FWHM is the one that represents the core itself, at the origin of the maps in Fig 4.4. Component 7, mentioned above, is seen to vary in position along the region of more diffuse intensity.

Tab. 4.3 overleaf shows the component parameters returned from the MODELFIT command in DIFMAP. The Flux (Jy) values correspond to the integrated flux in the circular gaussian components. The positions of the centroids of the circular gaussian components of major axis $\mathrm{B}_{\mathrm{major}}$ are expressed through the polar coordinates r (mas) and θ. From converting these coordinates to x and y coordinates and correcting for core position oscillation as described above, the values of x_{corr} and y_{corr} are obtained. From these corrected values, the value of the radial distance from the core component r_{corr} is calculated.

Ep.	Comp.	Flux (Jy)	r (mas)	θ	$\mathrm{B}_{\mathrm{major}}$	x_{corr}	y_{corr}	r_{corr}
1	1	0.405	0.011	175.3	0.038	0.000	0.000	0.000
	2	0.011	0.814	19.7	0.241	0.273	0.777	0.824
	3	0.021	1.353	20.8	0.151	0.479	1.276	1.363
	4	0.131	1.939	2.4	0.494	0.079	1.959	1.950
	5	0.018	2.539	–11.4	0.526	–0.502	2.500	2.550
	6	0.029	3.533	–4.8	0.824	–0.295	3.532	3.544
	7	0.016	6.004	8.7	2.600	0.907	5.946	6.015
	8	0.049	9.691	19.7	1.828	3.264	9.136	9.701
2	1	0.441	0.004	–64.4	0.035	0.000	0.000	0.000
	2	0.108	0.682	20.8	0.309	0.245	0.635	0.681
	3	0.27	1.304	20.4	0.154	0.467	1.217	1.304
	4	0.131	1.969	2.4	0.523	0.085	1.966	1.968
	5	0.017	2.666	–11.0	0.514	–0.505	2.615	2.663
	6	0.030	3.586	–5.1	0.847	–0.315	3.570	3.584
	7	0.016	5.683	6.8	2.600	0.676	5.642	5.682
	8	0.051	9.678	19.6	1.844	3.247	9.116	9.677
3	1	0.338	0.004	9.3	0.011	0.000	0.000	0.000
	2	0.008	0.555	25.6	0.113	0.239	0.497	0.551
	3	0.038	1.295	21.2	0.054	0.467	1.203	1.291
	4	0.112	1.994	3.1	0.557	0.107	1.987	1.990
	5	0.022	2.825	10.1	0.601	–0.498	2.777	2.821
	6	0.022	3.788	–4.5	0.820	–0.299	3.772	3.784
	7	0.016	5.608	6.9	2.600	0.675	5.563	5.604
	8	0.045	9.694	9.4	1.813	3.215	9.141	9.690
4	1	0.554	0.010	–156.2	0.020	0.000	0.000	0.000
	2	0.017	0.341	16.8	0.230	0.103	0.3350	0.350
	3	0.072	1.331	21.5	0.257	0.493	1.247	1.341
	4	0.092	2.018	3.5	0.535	1.28	2.0232	2.027
	5	0.024	2.567	–11.7	0.581	–0.516	2.523	2.575
	6	0.031	3.696	–4.6	0.936	–0.292	3.6932	3.705
	7	0.014	5.837	10.0	2.600	1.013	5.7576	5.846
	8	0.050	9.646	19.5	1.921	3.224	9.10162	9.656
5	1	0.525	0.006	–157.1	0.009	0.000	0.000	0.000
	2	0.0117	0.492	21.0	0.056	0.179	0.466	0.499
	3	0.090	1.370	22.3	0.263	0.522	1.274	1.377
	4	0.081	1.985	4.2	0.574	0.147	1.985	1.991
	5	0.027	3.915	–9.7	0.680	–0.462	2.731	2.770
	6	0.027	3.915	–3.1	1.008	–0.207	3.916	3.921
	7	0.016	6.716	7.9	2.600	0.924	6.659	6.723
	8	0.046	9.652	20.0	1.834	3.303	9.076	9.658
6	1	0.3820	0.0899	179.1	0.004	0.000	0.000	0.000
	2	0.1218	0.1817	1.9	0.170	0.005	0.272	0.272
	3	0.09853	1.3574	22.9	0.300	0.529	1.340	1.440
	4	0.0749	1.9090	5.2	0.597	0.172	1.991	1.998
	5	0.0321	3.920	–9.0	0.867	–0.445	2.875	2.909
	6	0.0229	3.9208	–3.4	0.927	–0.232	4.004	4.011
	7	0.0153	5.3971	10.6	2.600	0.991	5.395	5.485
	8	0.0522	9.535	20.0	2.021	3.247	9.054	9.619

Table 4.3: Component parameters of the MODELFIT process. See preceeding page for parameter details.

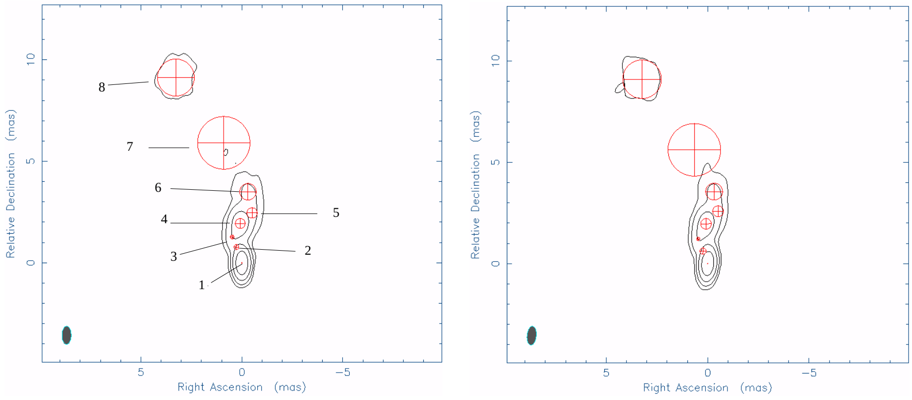

(a) 03/06/2009 (b) 19/08/2009

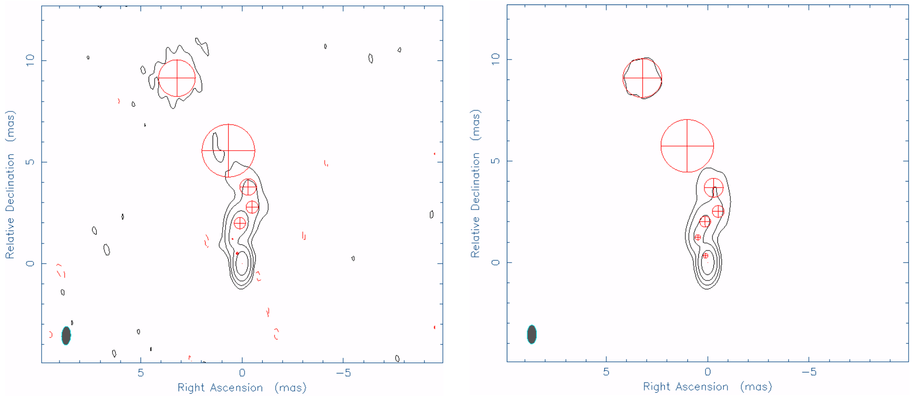

(c) 10/03/2010 (d) 27/09/2010

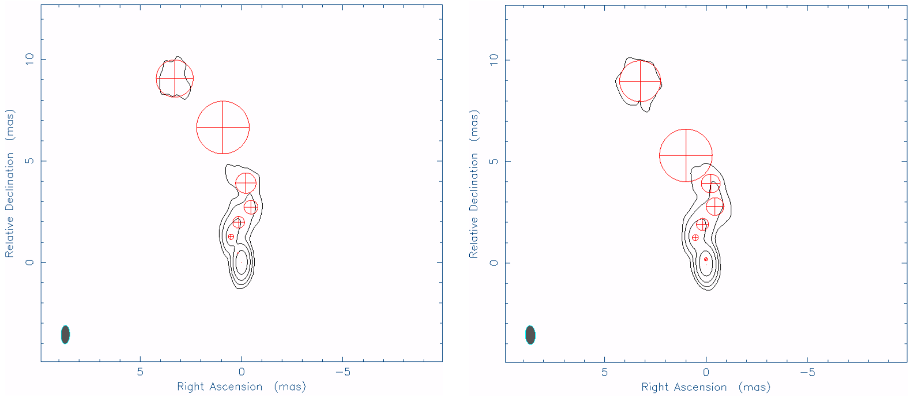

(e) 11/04/2011 (f) 29/04/2012

Figure 4.4: Maps of the source showing the circular gaussian model components for Epochs 1-6 ((a)-(f)). The component numbers are labelled in the image of Epoch 1. The smallest component is that of the core (Component 1).

4.3 Jet Emission and Kinematics

4.3.1 Kinematics of Jet Features

In order to calculate the apparent velocity of the components across the epochs, it is first necessary to relate the angular displacement of a source across the celestial sphere to the apparent transverse distance travelled. The derivation of this conversion is shown below.

The luminosity distance, D_{L}, of a source is related to its the angular size difference, D_{a}, by

$$D_{\mathrm{L}} = (1+z)^2 D_{\mathrm{a}} \tag{4.1}$$

where z is the redshift of the source. The angular size distance D_a is defined as the ratio of an objects physical transverse size to its angular size in radians,

$$D_{\mathrm{a}} = \frac{l}{\Delta\theta}. \tag{4.2}$$

Where l is the object's transverse size. Through the small angle approximation this becomes

$$D_{\mathrm{a}} = \frac{l}{\theta}. \tag{4.3}$$

The proper motion of the source, μ, in the the rest frame of the source is defined as

$$\mu = \frac{\Delta\theta}{\Delta t} \tag{4.4}$$

where $\Delta\theta$ is the change in angular displacement across the celestial sphere in time Δt. Multiplying the proper motion μ by the angular size distance D_{a} given in Equation (4.2) yields the transverse velocity $V_{\perp}$, measured in the source frame.

$$V_{\perp} = \mu D_{\mathrm{a}} = \frac{\Delta\theta}{\Delta t}\frac{D_{\mathrm{L}}}{(1+z)^2} \tag{4.5}$$

using the definition of D_{L} given in Equation (4.1). In the frame of the observer however, due to cosmic time dilation, the observed time interval will be $(1+z)\Delta t$, leading the expression of the apparent transverse velocity in the observers frame, given as V_{app}

$$V_{\mathrm{app}} = \frac{\mu D_{\mathrm{L}}}{(1+z)}. \tag{4.6}$$

In the kinematic analysis of the jet components, the proper motion is expressed in units of mas/year, therefore, a conversion factor of 1 mas/year $= 1.54 \times 10^{-16}$ rads^{-1} is included in order to express the velocities in ms^{-1}. The transverse velocity Equation (4.6) is therefore expressed in ms^{-1} by

$$V_{\mathrm{app}}[\mathrm{ms}^{-1}] = \frac{\mu[\mathrm{mas/year}] \times D_{\mathrm{L}}[\mathrm{pc}] \times 1.54 \times 10^{-16}[\mathrm{rads}^{-1}] \times 1\mathrm{pc}[\mathrm{ms}^{-1}]}{1+z} \tag{4.7}$$

The values of luminosity distance and redshift were taken from the MOJAVE data archive and are 9280 Mpc and 1.308 respectively[3]. The calculation yields

$$V_{\mathrm{app}}[\mathrm{ms}^{-1}] = \mu[\mathrm{mas/year}] \times 1.91 \times 10^{10}. \tag{4.8}$$

---

[3] assuming H_0=71 kms^{-1}Mpc^{-1}, $\Omega_\Lambda = 0.73$, $\Omega_m = 0.27$

Dividing by c yields the apparent velocity β_{app}

$$\beta_{\text{app}} = \mu[\text{mas/year}] \times 63.667. \tag{4.9}$$

The radial distance of the components from the core over the 6 Epochs is shown in Fig 4.5

The graph was created with the OpenOffice spreadsheet package. A linear regression fit was added for each component. The gradients of the linear regressions are shown in Tab. 4.4. The gradient of the lines represents the proper motion of the components μ as defined in Equation 4.4. From this gradient the values of β_{app} were calculated using the relation given in Equation 4.9.

The error on the linear regression was also calculated in the OpenOffice package using the LINEST function. These error values were converted linearly to give the error in β_{app} which are shown in Tab. 4.4.

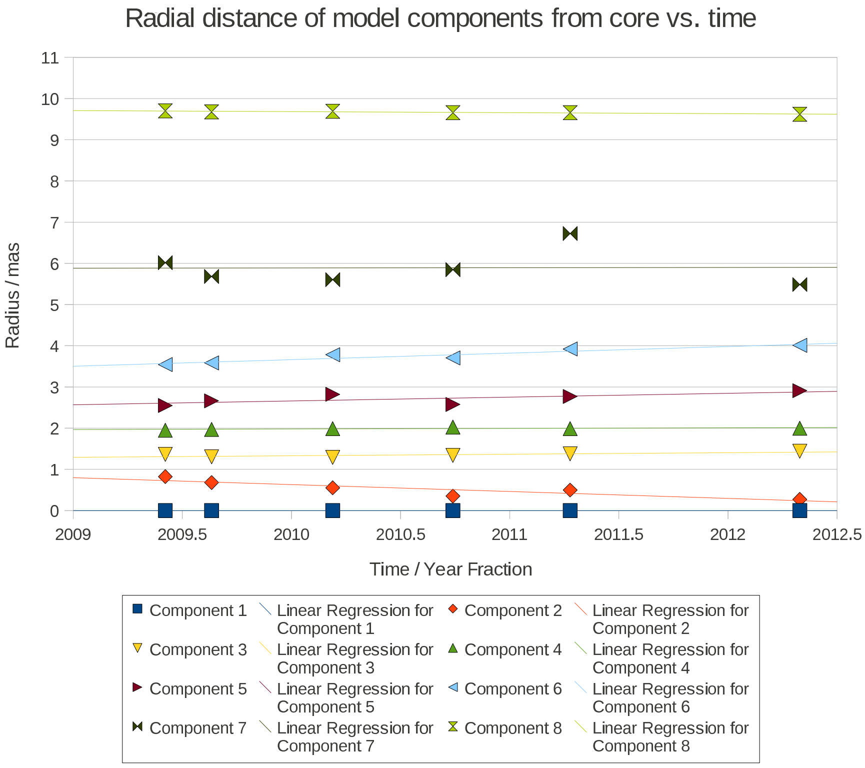

Figure 4.5: The radial separation of the model components from the core against time. The gradient of the linear regression represents the proper motion of the jet feature in units of mas/year.

Within the error ranges, Components 3, 5, and 6 show definite superluminal motion as given in Tab. 4.4. Component 7 shows a very large error margin, reflecting it *non-robust* characteristics. Components 2 and 8 show negative apparent velocities. A negative apparent velocity describes the motion of a jet feature towards the core. Such motion is non-physical due to the emission

Component	μ	σ_μ	$\beta_{\text{app}} \pm \sigma_{\beta_{\text{app}}}$
1	0	0	0 ± 0
2	-0.167	0.043	-10.63 ± 2.7
3	0.038	0.015	2.42 ± 1.0
4	0.015	0.010	0.96 ± 0.6
5	0.093	0.046	5.92 ± 2.9
6	0.160	0.028	10.19 ± 1.8
7	0.005	0.205	0.32 ± 13.1
8	-0.025	0.005	-1.59 ± 0.3

Table 4.4: The values and errors of the proper motion,μ and σ_μ respectively, derived from the gradient of the linear regression of the componets in Fig 4.5. The values of the apparent velocity β_{app} the error in the apparent velocity, $\sigma_{\beta_{\text{app}}}$, are obtained through the conversion given in Equation 4.9.

mechanisms and properties of jets in AGN and the observed values may arise from reasons discussed in Section 5.1.

Viewing Angle

The angle which the jet makes with the line of sight of the observer can be calculated through the relations given in Section 2.2.2. From Equation (2.8) we see that the maximum apparent velocity $\beta_{\text{app}_{\text{max}}}$ is given by

$$\beta_{\text{app}_{\text{max}}} = \frac{\beta}{\sqrt{1-\beta^2}}. \tag{4.10}$$

From Equation (2.7) we see that $\cos\theta_{\text{max}} = \beta$ where θ_{max} is the maximum viewing angle and β is the true velocity of the component. Through substituting this relation into Equation (4.10) we obtain

$$\beta_{\text{app}_{\text{max}}} = \frac{\cos\theta_{\text{max}}}{\sqrt{1-\cos^2\theta_{\text{max}}}} = \frac{\cos\theta_{\text{max}}}{\sin\theta_{\text{max}}} = \frac{1}{\tan\theta_{\text{max}}}. \tag{4.11}$$

From which we see that

$$\theta_{\text{max}} = \tan^{-1}(\frac{1}{\beta_{\text{app}_{\text{max}}}}). \tag{4.12}$$

The maximum observed apparent velocity of a jet component in B1551+130 was that of Component 6 of value β_{app}=10.19 as shown in Tab. 4.4.

By substitution into Equation (4.12) the maximum viewing angle is calculated as

$$\theta_{\text{max}} = 5.6^\circ \tag{4.13}$$

To estimate the error on this value, we take the error in β_{app} of ±1.78 as given in Tab. 4.4. The value of the viewing angle is then calculated for the for an apparent velocity of 10.19+1.78=11.97 and for 10.19–1.78=8.41. This yields the viewing angles of 4.78° and 6.78° respectively. The maximum variation of these values from the value calculated in Equation (4.2) is 6.78°–5.61°=1.17°.

Therefore the value of the viewing angle is given as

$$\theta_{\text{max}} = 5.6 \pm 1^\circ \tag{4.14}$$

This small viewing angle is concordant with the classification of B1551+130 as a Blazar.

4.3.2 Flux of Jet Features

The flux values returned in DIFMAP after every MODELFIT represent the integrated flux of the pixels 'underneath' the gaussian model component. The logartimic scale in Fig. 4.6 allows an effective visualisation of the flux variations across the epochs as on a linear scale the plot would be dominated by the high flux of the core. The most striking feature in Fig. 4.6 is the huge increase in flux of Component 2 between Epochs 5 and 6 (discussed in Section 5.1). Component 3 shows a steady increase in flux over the 6 epochs as does Component 5 between Epochs 2 and 6. Component 4 shows a steady decrease in flux. The proportional fluctuations in the flux of Components 1, 6, 7, and 8 show no clear trend.

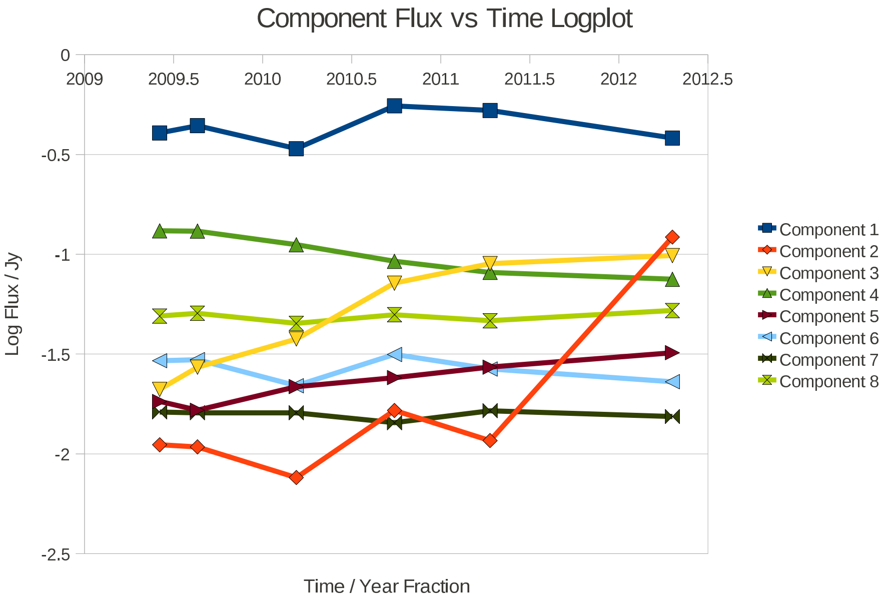

Figure 4.6: The logarithm (base 10) of component flux plotted against time. The same plot on a non-logarithmic scale can be found in Section 5.2 (Fig. 5.3)

Luminosity Doppler Boosting

The luminosity Doppler boosting factor as given in Equations (2.1) and (2.2) can be calculated for the source using the intrinsic velocity β given by

$$\beta = \cos\theta_{\max} = 0.995217, \tag{4.15}$$

with $\theta_{\max}$ given in Equation (4.13). Using Equation (2.2) the Doppler factor, δ^n is simply given by

$$\delta^n = (\frac{\sqrt{1-\beta^2}}{1-\beta^2})^n = \gamma^n \tag{4.16}$$

The value n depends the geometry and spectral index of the source and typically lies between a value of 2 and 3 [19]. Taking $n = 2$ we obtain a lower estimate of the Doppler boosting factor

$$\delta^n = \gamma^n \approx 10^2 \tag{4.17}$$

where the Lorentz factor γ was approximated as 10 for $\beta = 0.995217$ as given in Equation (4.15). We therefore conclude that through Doppler boosting effects, the intrinsic luminosity of the source is amplified by a factor of the order 10^2.

Chapter 5

Discussion

5.1 Component Behaviour

Since this is the first detailed analisis of pc-scale structure of this source, there are no earlier studies to compare with our results.

Along with the emission properties of this source and its one-sided kpc-scale morphology, the result obtained for the viewing angle of 5.6° ± 1° agrees with the classification of B1551+130 as a blazar. Superluminal velocites of knots are observed in the jet, with a maximum value of 10.2±1.8c and such velocities would be expected from an AGN jet orientated at such a small angle to the line of sight. However, there remain results which merit further analysis. Negative superluminal motion was observed in two components: in Component 2 with a value of -10.6 ± 2.8c, and in Component 8 with value of -1.6 ± 0.3c. Additionally, the flux of Component 2 rises sharply in the last epoch.

5.1.1 Inward Feature Motion?

Negative superluminal motions have been observed in the kinematic analysis of other AGN jets (e.g., [18], [24]) and apparent inward motion can arise for a number of reasons given below.

- In large diffuse features, internal brightness fluctuations can cause the centroid of the gaussian to change position, possibly simulating inward motion of the feature. Additionally, knots which show no significant motion can be subject to position oscillations which can lead to negative velocities being observed.

- It is possible that due to absorption, the true core of the jet is not seen and the motion of the jet features is measured against another moving feature. This means that any knot along the jet which is moving outwards at a slower pace that the reference feature will appear to be moving inwards.

- In highly curved jets, any feature which is moving away from the core and bends back towards the line of sight will appear to be moving inwards when infact its separation from the core is increasing.

- The illusion of apparent inward motion could also be due simply to patterns in the flow along the jet and that no distinct features are moving inwards.
- If a new feature which emerges from the core is not resolved by the beam, the position of the core will shift slightly towards the components along the jet. This means that with respect to the core the jet features can appear to be moving inwards.

As evident in Figs. 4.3 and 4.4 Component 8 represents a large area of reasonably diffuse flux. As stated, such areas can be subject to changes in the internal intensity distribution which cause the position of the centroid of the circular gaussian component to change over time with a net inwards motion. The magnitude of the velocity is one of the lowest measured in the jet which would also strengthen the case for the negative apparent motion being due to internal brightness variations rather that a definite inwards motion of the whole feature.

5.1.2 The Core Region

As detailed in Tab. 4.3, the separation of Component 2 from the core decreases from a value of 0.50 to 0.27 mas between Epochs 5 and 6. It must be noted however that self-calibration removes any absolute positional information from the data. Throughout the epochs the core is taken as the (assumed) stationary reference position from which to measure the movement of the jet features. However, as stated above, a feature that is emitted from the core which is unresolved will shift the position of the centroid of the core component in the direction of the jet flow, decreasing the apparent outwards velocity of more distant components, or indeed causing them to show inward motion. If this hypothesis were applied to the object of study however, it would remain to be explained why only Component 2 shows such high negative superluminal motion unlike other features which exhibit more realistic outward motion.

If we assume Component 2 to be intrinsically quasi-stationary, the observed velocities of the other jet features would be around 10c less than their true apparent velocities. If we take into consideration that the distribution of apparent velocities of propagating jet features in blazars peaks at 10c and extends to 50c ([16]), the true apparent velocities implied by this hypothesis are viable. Additionally, were this to be the case, the maximum apparent velocity of Component 6 which was used to calculate the viewing angle would be around 20c, giving a value for the viewing angle of $\approx 2.9^\circ$ in line with the value of 3° calculated by Ghisellini et al ([11]) using methods which do not involve the kinematic analysis of jet features.

It could be argued that assuming a feature so close to the core to be quasi-stationary is not a realistic assumption. It must be noted however that Component 2 was the second last component to be added to the model and its flux values before Epoch 6 were the lowest out of all the other components, calling into question its reliability as a model component representing a knot emitted from the core. Were it possible to estimate the error on the model component parameters, a more quantative approach could be used to judge the reliability of Component 2, however such error analysis is difficult due to non-linear dependencies in the (u, v) plane coverage and thermal noise among other factors and is beyond the scope of this project. Previous error analysis on gaussian model components give uncertaintes in parameters of brightest components as being smaller by a factor of around 2 [15].

Between Epoch 5 and 6 the flux of Component 2 increases by a factor of over 10 and its separation from the core decreases from 0.50 to 0.27 mas. Were Epoch 6 the first epoch to be viewed, Component 2 would almost certainly be assumed to be a jet feature recently emitted from the core. From observations at 2 cm, we get little insight into emission at the base of the jet, the mm-wave core as shown in Fig. 2.3. A newly emerging component would begin in the base of the jet where the opacity is such that it would be invisible at radio wavelengths. As the component travels through the jet its observed radio flux will increase unil it emerges fully from the core and is fully visible at radio wavelengths.

It would be very interesting to view the jet at mm wavelenths to try to ascertain whether a newly emerging component may influence the motion of Component 2, or indeed whether Component 2 in Epoch 6 represents this newly emerging component. If this is the case however, one would have to find a physical argument to justify a component of small flux moving towards the core before the emergence of a new knot, and then this same (previously weak) model component increasing in flux and representing the emerging feature. If observations of future epochs showed the outward (possibly superluminal) motion of this component it would point to this being the case.

In order to test that a feature that *could* be resolved by the beam had not emerged in the previous epochs, the model fitting process was carried out again over the epochs but this time without using the saved models from the anterior epoch. Through this method it was hoped that any new component that was resolved by the beam would show up as a bright area on the dirty map instead of the existing components changing position to 'cover' the the increased flux. The results using this method largely followed those obtained through the original process of using the saved models.

Additionally, the model fitting was carried out again using an elliptical gaussian to model the core. It was hoped that the extra variable parameter of the core model component would model it more effectively and possibly alter behaviour of Component 2. However, the results from this method did not show any significant differences that those obtained from the original process.

Explaining the behaviour of this component, especially in the last epoch presents an interesting challenge although unfortunately, with the data available it is difficult to propose the most likely hypothesis with any degree of certainty. Were it possible to view the source at mm wavelengths we could know more about emission from the core which would provide more data from which to assess the likelihood of a new feature emerging in Epoch 6. Oncoming, already granted MOJAVE VLBI observations will also provide extra information from which to form a more accurate hypothesis.

5.2 B1551+130 at Other Wavelengths

5.2.1 SED

To complement the analysis at radio wavelenghts, the spectral energy distribution (SED) of the source is also presented. This SED was built using the ASDC

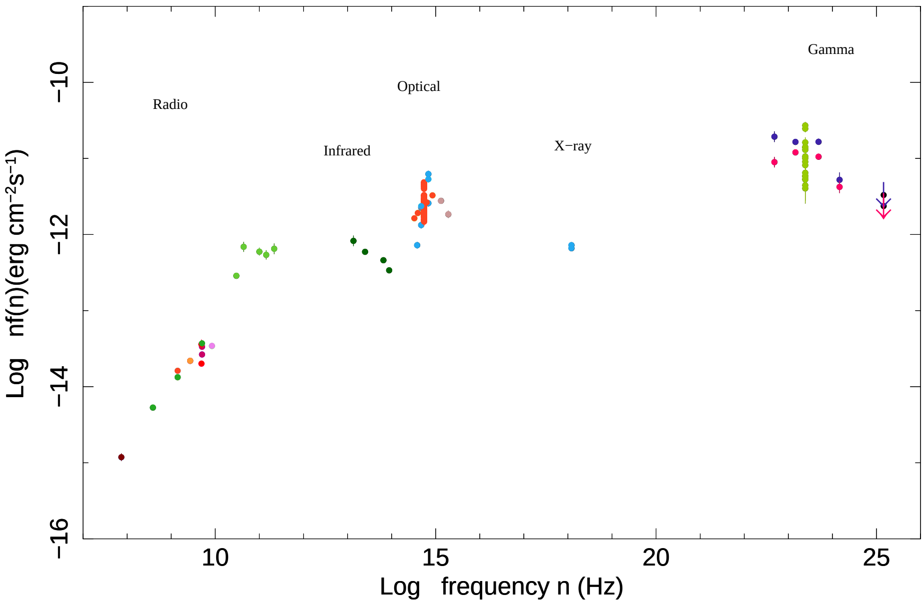

Figure 5.1: The spectral energy distribution for B1551+130. Data by *Swift* (analysed in IRAM by C.S. Chang, priv. comm.) and the ASDC SED tool (rest of instruments). Figure produced by E. Ros (priv. comm.) using the QPD software available at Bamberg Observatory. The bands of the EM spectrum corresponding to each group of data points are labelled.

online SED tool[1] which loads data from various catalogues of surveys at different frequencies. When the data is loaded the program also allows polynomial fits to be added and parameters extracted from them. In depth analysis of the SEDs of a sample gamma-loud blazars can be found in [2].

The SED allows a visual representation of the strength of emission of a source in different bands of the EM spectrum. The SED in Fig. 5.1 plots the logarithmic spectral luminosity against logarithmic frequency. Data points of the same colour were detected by the same survey and distinct groups of points can be noted, corresponding to observations in distinct spectra. These spectral bands are highlighted in Fig. 5.1. The maximum value of a polynomial made to fit the radio and infrared points is know as the *syncrotron peak*. This peak corresponds to the frequency bin at which the non-thermal syncrotron emission from the core and the jets of the AGN is highest. Similarly, the maximum value of a polynomial made to fit the X-ray and gamma points will yield the *compton peak*. It is proposed that the upscattering of the syncrotron radiation photons through the inverse Compton effect gives rise to the thermal radiation resposible for this second 'hump' on the SEDs of blazars [39].

Using the ASDC SED tool, a third order polynomial representing the syncrotron hump was drawn, yielding a maximum value of $10^{12.47}$ Hz. [2] find the synctrotron peak frequencies for FSRQs to range between $10^{12.5}$ to $10^{14.5}$. It is difficult to estimate the error margins on the value calculated for the object of study as it would be influenced the uncertainties on all data points obtained

---

[1] http://tools.asdc.asi.it/SED/

through different surveys. However it is likely that the appropriate errors margins would allow for the calculated value to lie within the range given in [2].

5.2.2 γ-Emission

The gamma emmission of the source between 06/03/2009 and 06/03/2012 as detected by the by the Large Area Telescope onboard the *Fermi Gamma-Ray Space Telescope*, (*Fermi*/LAT), is shown in Fig. 5.2. The points represent the integrated flux over a 30 day period with energy range of 1-300 Gev. Fig. 5.3 shows the flux of the MODELFIT method model components on a linear scale.

Investigating the relation between the strength of radio and gamma emission in AGN jets is a very active research field within radio astronomy. It was found in [21] that a an AGN was likely to show increased radio emission typically a few months after a flare in gamma. It was also found that the jet core would be the most likely location for this flaring.

A rigourous comparison between the gamma and radio emission for the source would involve correlating the light curves is Figs. 5.2 and 5.3 using an appropriate correlation function. Such analysis is beyond the scope of this report although a visual comparison would serve to identify any obvious correlations.

In the *Fermi* light curve in Fig. 5.2, the large error margins on many points make it hard to identify a general trend in the gamma emission of the source. The low-error points from 2010.7 onwards show the source has high gamma variability with a slight period of increased emission between 2011.6 and 2011.8. Additionally, the emission rises to the highest level over the period of observation at around 2010.3 after following a steady increase from around 2010.0. Even within the large error margins this point corresponds to a strong peak in gamma emission before following a decreasing trend until 2010.8.

By taking into consideration the typical delay in the observation of increased radio emission after a gamma flare found in [21], we would expect to note a radio flare at around 2010.5. From Fig. 5.3 we see the radio emission of the core (Component 1) rises sharply between 2010.3 and 2010.7 before decreasing steadily thereafter. These observations seem to provide evidence for increased radio emission being obseved after periods of increased gamma emission for this source. However, due to the relatively long time periods bewteen the VLBI radio observations, it is difficult to identify with certainty any correlation between the emission in radio and gamma. It must be stressed that these results can only serve to identify a possible correlation which would be could be analysed more rigourously were more time available.

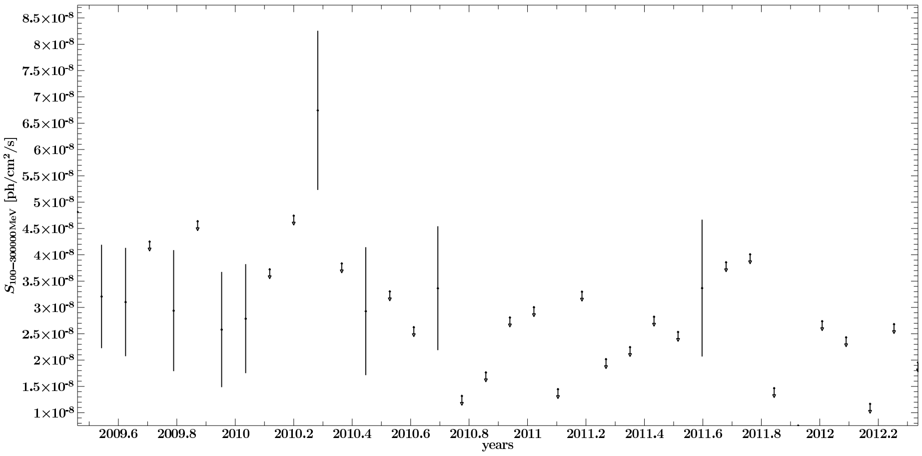

Figure 5.2: Light curve provided by C. Müller (priv. comm.). Gamma emission detected by the *Fermi* Large Area Telescope between March 2009 and March 2012. Each point represents the flux integrated over 30 day periods. Arrows represent upper limits to the flux. Notice the very significant gamma-flare in early 2010.

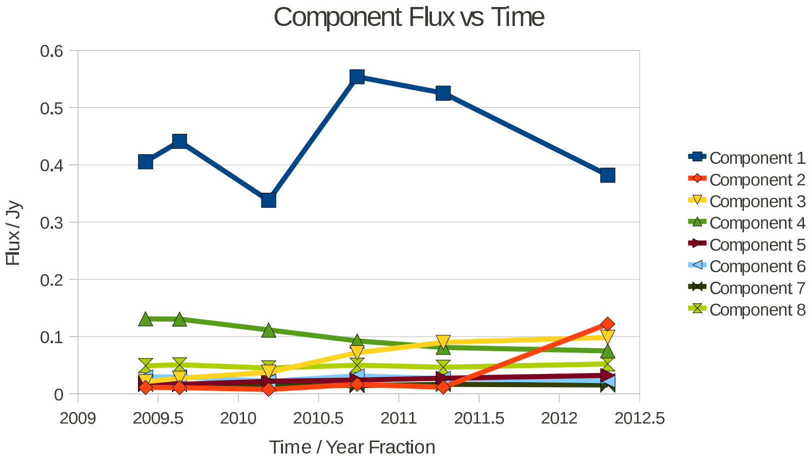

Figure 5.3: The flux of the jet model components over time. The linear scale serves to accurately represent the variations in the strength of radio emission from the core (Component 1).

Chapter 6

Summary and Concluding Remarks

The field of radio astronomy has come a long way since Jansky' first observation of galactic radio emission in 1933. Through the advancement of aperture synthesis techniques, the most energetic structures in our universe can be imaged with sub-milliarcsecond resolution. Radio interferometry has allowed us to look back billions of years into the universe's past to explore objects of unimaginable size and power.

In this report, the relativistic jet of the flat spectrum radio quasar B1551+130 was analysed using VLBI data taken over 6 epochs between June 2009 and April 2012 in the MOJAVE 2 cm survey. Maps of the radio brightness of the source were created in DIFMAP through the CLEAN deconvolution algorithm whilst using phase selfcalibration to improve the modeled visibilities.

Through the gaussian model fitting technique, the kinematic analysis of the relativistic jet was carried out. This allowed the position and flux of knots in the jet, modeled by circular gaussian components, to be tracked over the epochs of observation. The apparent velocities of the jet components were calculated by taking the gradient of the linear regression fit of the component position plotted against time. The apparent velocities measured ranged from 10.2±1.8c to 1.0±0.6c. The superluminal motion of these components arise from the relativistic effects associated with viewing AGN jets at a small angle to the line of sight. From the maximum apparent component velocity, the maximum viewing angle was calculated to be $5.6^{\circ} \pm 1^{\circ}$, in line with the classification of B1551+130 as a flat spectrum radio quasar. The luminosity boosting factor was also estimated to be of order 10^2

Component 2 was observed with high negative superluminal motion of -10.6 ± 2.7c and showed a large flux increase in between Epochs 5 and 6. Such motion cannot correspond to the inward motion of plasma, but can be explained by several effects which would give the appearce of enhanced radio emission moving backwards in the relativistic stream.

A newly emerging component which is not resolved could shift the reference component (core) in such a way that the velocities of the jet features appear to moving more slowly and in some cases inwards. There is no observational evidence to prove this is the case in the object of study however.

Additionally, the large flux and close proximity to the core of Component 2 in Epoch 6 is compatible with this component representing a newly emerging feature. In this case however, the inward motion of this same component before Epoch 6 remains to be explained.

In order to know more about the processes which give rise to the behaviour of this component it would be extremely valuable to be able to view the source at mm wavelengths, that is, accessing the regions closer to the central engine which are self-absorbed at 2 cm wavelenghts as used in this study. Oncoming VLBI observations will also be important in determining whether Component 2 in Epoch 6 represents a newly emerging feature.

The gamma light curve presented in Section 5.2 was also compared with the flux of the core. A non-rigourous comparison provided evidence for a correlation between radio and gamma flares between 2010 and 2011. Were more time available it would be interesting to quantify the correlation mathematically and continue this comparison as more gamma and radio emission data becomes available.

The multi frequency analysis of AGN will be performed with increased resolution in the coming years through projects such as SKA and ALMA. VLBI methods are also continuously evolving and will benefit from the development of eVLBI. One of the most remarkable properties of AGN is their spectral range of emission, and through complementing the efforts of radio astronomy with observations across the EM spectrum, we will build up an ever more accurate picture of the emission processes governing these fascinating objects.

Bibliography

[1] Abdo A.A. et al., 2010, Astrophys. J. Suppl. Ser., Vol. 188, p. 405.

[2] Abdo A.A. et al., 2010, Astrophys. J., Vol. 716, p.30.

[3] Baade W., Minowski R., 1954, Astrophys. J., Vol. 119, p. 206.

[4] Bicknell G., 'Parsec scale properies and unified schemes', Radio Galaxies Lecture 2.

`http://www.mso.anu.edu.au/newcosmology/lectures/Bicknell_radiogals2.pdf`.

[5] Bridle A.H. et al, 1994, Astronom. J., Vol. 108, p. 766-820.

[6] Burke B.F., Graham-Smith F., 2010, 'An Introduction to Radio Astronomy', 3rd edition, Pub. Cambridge University Press.

[7] Clark B.G., 1982, 'Large Field Mapping', Lecture 10 in the NRAO-VLA Workshop on "Synthesis Mapping", Ap., Vol. 89, p.377-378.

[8] Digitised Sky Survey, Space Telescope Science Insitute.

`archive.stsci.edu/`

[9] Falla D.F., Floyd M.J., 2002, European Journal of Physics, Vol. 23, p. 69-81.

[10] Fanaroff B.L., Riley J.M., 1974, MNRAS, Vol. 167, p.31P-36P.

[11] Ghisellini G. et al., MNRAS, Vol. 399, p. 2041-2054.

[12] Hey J.S., et al, 1946, Nature, Vol. 158, p. 234.

[13] Högbom J.A., 1974, Astron. Astrophs. Suppl., Vol. 15, p. 417-426.

[14] Hogg D.W., 2000, 'Distance measures in cosmology', arXiv:astro-ph/9905116.

[15] Homan D.C. et al., 2002, Astrophy. J., Vol. 568, p. 99-119.

[16] Homan D.C., 2012, International Journal of Modern Physics: Conference Series, Vol. 8, p. 163-171.

[17] Hovatta T. et al., 2009, Astron. and Astrophys., Vol. 494, n. 2, p. 527-537

[18] Jorstad S.G., Marscher A.P., 2006., 'Blazar Variability Workshop II: Entering the GLAST Era', eds. H. R. Miller, K. Marshall, J. R. Webb, M. F. Aller, ASP Conference Series, Vol. 350.

[19] Kellerman K.I. et al, Astrophys. and Space Sci. Vol. 311, 1-3, p. 231-239.

[20] Kovalev Y.Y., 2009, ASP Conference Series, Vol. 402, p. 179-183.

[21] Kovalev Y.Y. et al, 2009, Astrophys. J. Lett. Vol. 692, L17-L21.

[22] Laing R.A., Bridle A.H., 1987, MNRAS (ISSN 0035-8711), Vol. 228, p. 557-571.

[23] Lister M. et al., 2009, Astrophys. J., Vol. 137, p. 3718. MOJAVE Data Archive,

`http://www.physics.purdue.edu/astro/MOJAVE/allsources.html`

[24] Lister M.L. et al., 2009, Astronom. J., Vol. 138, p. 1874.

[25] Ma C. et al., 1998, Astronom. J., Vol. 116, p. 516.

[26] Martí Vidal I., 2008., 'Expansion de SN 1993J y Astrometria Global de Alta Precision', Doctoral Thesis.

[27] Marscher A.P., 2006, American Institute of Physics Conference Series, eds. P.A. Hughes and J.N. Bregman, Vol. 856, p. 1-22.

[28] National Radio Astronomy Observatory, `www.nrao.edu`.

[29] Padovani P., 1999, 'Frontier Objects in Astrophysics and Particle Physics', eds. F. Giovannelli and G. Mannocchi G., SIF, Vol. 65, p. 159.

[30] Ros E., 2008, Journal of Physics: Conference Series Vol. 131, 012061

[31] Ros E., 2012, 'High-resolution of monitoring of parsec-scal jets in the fermi era', Proceedings of Fermi and Jansky: Our Evolving Understanding of AGN, eConf C1111101.

[32] Ruszkowski M., Begelman M. C., 2002, Astrophs. J, Vol. 573, p.485.

[33] Schönfelder V. Ed., 2001, 'The Universe in Gamma Rays', pub. Springer.

[34] Shepherd M.C. et al., Bull. Astron. Soc., Vol. 26, No. 2, p. 987-989.

[35] Smith F.G., 1951, Nature, Vol. 168, p. 962.

[36] Thomson A.R., Moran J.M., Swenson Jr. G.W., 2001, 'Interferometry and Synthesis in Radio Astronomy', 2nd Edition, Pub. Wiley-VCH.

[37] Urry C.M., Padovani P., 1995, Publ. Astron. Soc. Pacific., Vol. 107, p. 803.

[38] Verschuur G.L., Kellermann K.I. eds., 1988 'Galactic and Extragalactic Radio Astronomy', 2nd Edition, Springer-Verlag.

[39] Weidinger M. et al., Astrophs. Space Sci. Trans., Vol. 6, p. 1-7.

[40] Wilms J., Kadler M., 2010, 'Multi-Wavelength Astronomy'

`http://pulsar.sternwarte.uni-erlangen.de/wilms/teach/agn`.

[41] Wilner D.J., 2010, 'Imaging and Deconvolution', NRAO 12th Synthesis Imaging workshop.

`http://www.aoc.nrao.edu/events/synthesis/2010/lectures10.html`.